Sea-ice drag as a function of deformation and ice cover: Effects on simulated sea ice and ocean circulation in the Arctic.

GIULIA CASTELLANI[a,*], Martin Losch[a], Mischa Ungermann[a], Rüdiger Gerdes[a]

[a] *Alfred Wegener Institute Helmholtz Centre for Polar and Marine Research, Am Handelshafen 12, D-27570 Bremerhaven, Germany.*

Abstract

Many state-of-the-art coupled sea ice-ocean models use atmospheric and oceanic drag coefficients that are at best a function of the atmospheric stability but otherwise constant in time and space. Constant drag coefficients might lead to an incorrect representation of the ice-air and ice-ocean momentum exchange, since observations of turbulent fluxes imply high variability of drag coefficients. We compare two model runs, one with constant drag coefficients and one with drag coefficients varying as function of sea-ice characteristics. The computed drag coefficients fall in the range of observed values and show the interplay of ice deformation and ice concentration in different seasons and regions. The introduction of variable drag coefficients improves the realism of the model simulation. In addition, using the average values of the variable drag coefficients improves simulations with constant drag coefficients. When drag coefficients depend on sea-ice characteristics, the ice moves faster and this leads to a reduction of ice thickness in the entire Arctic and particularly in the Lincoln Sea. Variable drag coefficients lead also to a deeper mixed layer in summer and to changes in surface salinity and temperature in the ocean. Small effects are visible also in the ocean interior.

*Corresponding author. *E-mail address:* giulia.castellani@awi.de

1. Introduction

The recently observed changes in Arctic sea ice (Rothrock et al., 1999; Serreze et al., 2003, 2007; Stroeve et al., 2007, 2012a,b; Laxon et al., 2013; Haas et al., 2008; Rabenstein et al., 2010; Castellani et al., 2014) feed back into the global climate because sea ice is coupled to atmosphere and oceans. Sea ice insulates the oceans from the polar atmosphere, it contributes to the ice-albedo feedback mechanism (Curry et al., 1995), and, while drifting, it exerts a drag on the oceanic surface layer. This drag fluxes momentum into the ocean. The momentum fluxes between ice and ocean affect the upper surface circulation with consequences for the interior ocean circulation and the outflow into the Nordic Seas as well as the Pacific and Atlantic Ocean. Understanding the dynamic coupling between ice, atmosphere and ocean requires a detailed representation of the momentum fluxes.

In this work, we aim to contribute to improving the representation of physical processes in coupled sea-ice–ocean models by investigating how numerical simulations are affected by a description of ice-atmosphere and ice-ocean coupling that accounts for the sea-ice roughness.

Most sea-ice codes resolve both dynamic and thermodynamic processes. The sea-ice momentum equation is solved for drift velocities that are then used to advect the ice variables. The drift velocities also determine the stress acting on the ocean. In most sea-ice models (Hibler, 1979; Hunke, 2010), both the atmospheric drag and the oceanic drag are described by a quadratic relationship (see also the Arctic Ocean Model Intercomparison Project -AOMIP- protocol, Proshutinsky et al., 2001) depending on the relative velocity between atmospheric wind (ocean currents) and sea-ice drift. The intensity of the air-ice and ocean-ice interactions are described by the transfer coefficients called air drag coefficient c_a and ocean drag coefficient c_w. These coefficients depend on sea-ice surface characteristics. Table 1 lists direct observations of atmospheric drag coefficients and indirect estimates from linear (Castellani et al., 2014) and 3D (Petty et al., 2017) surface profiles, all at a reference height of 10 m; and oceanic

drag coefficients that are generally referenced to geostrophic currents (Lu et al., 2011).

Many sea-ice models in coupled GCMs today use constant drag coefficients, thus they do not account for their observed spatial and temporal variability (Hunke et al., 2010). In recent years many parameterizations have been developed to relate sea-ice surface characteristics to drag coefficients (Garbrecht et al., 2002; Birnbaum & Luepkes, 2002; Lüpkes & Birnbaum, 2005; Lüpkes et al., 2012, 2013; Andreas et al., 2010; Lu et al., 2011), and some of these parameterizations have been implemented in numerical models. For example, Tsamados et al. (2014) present the results of a simulation with the Los Alamos sea-ice model CICE where some of the mentioned parameterizations are used to compute the atmospheric and oceanic neutral drag coefficients as a function of floe edges, ridges, and melt ponds. Moreover, CICE allows to include instability effects of the surface layer over sea ice, thus the neutral drag coefficients are corrected for the stability that depends on the thickness distribution and thus on the sea-ice surface state (Hunke et al., 2015). The approach of Tsamados et al. (2014) requires a dynamic ice thickness distribution (ITD) as well as an explicit description of ridges and melt ponds formation (Flocco & Felthman, 2007; Flocco et al., 2010). In a different approach (Steiner et al., 1999; Steiner, 2001), deformation energy accounts for surface roughness. The deformation energy depends on the history of the mechanical deformation of sea ice and on changes in its thickness. The drag coefficients are parameterized as a function of the deformation energy and of ice concentration (Steiner, 2001). With this formulation it is possible to implement drag coefficients in sea ice models without additional parameterizations for ridges and melt ponds formation.

Tsamados et al. (2014) and Steiner (2001) used stand alone sea ice models. But variations of oceanic drag coefficients also affect the oceanic momentum through the drag coefficients and the drift velocities of the ice that are themselves functions of the atmospheric and oceanic stress. For example, Castellani et al. (2015) showed, based on an idealized experiment, that variations in the Ekman vertical velocity associated with variable oceanic drag coefficients are

on the same order of magnitude as the variations due to changes in the surface velocity of the ice. Roy et al. (2015) compare simulations using different air-ice and ocean-ice roughness. They show effects on the general features of sea ice (concentration, thickness, drift) and also on the liquid and solid fresh water budget of the Arctic Ocean. In particular, increased ice-ocean roughness leads to higher Arctic fresh water budget by increasing fresh water retention in the Beaufort Gyre. Martin et al. (2014) investigate changes in momentum transfer to the ocean as consequence of ice thickness and areal extent decrease. They conclude that the weaker ice cover in fall, winter and spring, and the increase in open water fraction in summer cause trends in the momentum transfer over the last three decades. In a more recent work, Martin et al. (2016) analyze the effects that the introduction of variable drag coefficients in numerical models have on the trend of annual mean ocean surface stress. They show that a decrease in surface roughness over the years leads to a decline in surface ocean stress. They conclude that a proper investigation of the trend of the air to ocean momentum transfer in presence of sea ice requires to represent sea-ice surface variations.

In the present study we investigate how atmospheric and oceanic drag coefficients that depend on the degree of sea-ice deformation and on ice concentration affect sea-ice distribution and ocean circulation in a numerical model. We follow the Steiner (2001) deformation energy approach and apply it to a coupled sea ice-ocean model. We focus on the simulated sea-ice properties, but also on effects on and changes in the ocean circulation, with the aim to investigate (1) which of the main physical parameters describing the large scale sea ice cover (ice concentration, thickness and drift) is affected the most, and (2) in which regions of the Arctic these changes are more prominent. Finally, we aim to (3) quantify to what extent the ocean is affected.

In Section 2 we introduce the model configuration and the implemented parameterizations. We also describe the sensitivity study performed to select the set of parameters used in the numerical experiment. The results for sea ice and ocean are presented in Section 3 and then discussed in Section 4. A summary and conclusions follow in Section 5.

2. Methods

2.1. Model Description and Setup

We use the Massachusetts Institute of Technology general circulation model (MITgcm, Marshall et al., 1997) in a coupled ocean–sea-ice Arctic Ocean configuration. The configuration is similar to the NAOSIM configuration of Karcher et al. (2011) and was already described in Castro-Morales et al. (2014). The domain covers the Arctic Ocean, the Nordic Seas, and the North Atlantic down to approximately 50°N (Figure 1). The horizontal resolution of 1/4° corresponds to ∼28 km on a rotated spherical grid with the equator passing though the North Pole. In the vertical, the domain is discretized in 33 levels with thickness ranging from 10 m at the surface to ∼ 350 m at depth. Vertical mixing in the ocean is parameterized by a K-Profile Parameterization (KPP) scheme (Large et al., 1994) and tracers are advected with an unconditionally stable seventh-order monotonicity preserving scheme (Daru & Tenaud, 2004) that requires no explicit diffusivity. The mixed layer depth is parameterized based on a density criterion (Kara et al., 2000).

The ocean model is coupled with a dynamic-thermodynamic sea-ice model (Losch et al., 2010). The sea-ice model of the MITgcm uses a viscous-plastic rheology and so-called zero-layer thermodynamics (i.e., zero heat capacity formulation, Semtner, 1976) with a prescribed ice thickness distribution (Hibler, 1979, 1980, 1984; Castro-Morales et al., 2014): In order to compute the net heat flux through the ice, the latter is redistributed into seven ice thickness categories between 0 and a maximum thickness of twice the mean thickness. The heat fluxes are computed individually for each thickness and then summed. The shape of the distribution of these seven thicknesses is flat, normalized and fixed in time (see Hibler, 1984; Castro-Morales et al., 2014, their Figure 1). We also use the same parameterization for the snow distribution. In the present configuration the model does not include a dynamic ice thickness distribution (ITD).

The model is forced by realistic atmospheric fields. We use data of the

Coordinate Ocean Research Experiment (CORE) version 2 (Large & Yeager, 2009) for the spin-up and the NCEP Climate Forecast System Version 2 (Saha et al., 2014) for the analyzed simulations. A monthly climatology of river runoff for the main Arctic rivers follows the AOMIP protocol (Proshutinsky et al., 2001).

The model is spun up from the first day of January 1948 to the last day of December 1978 in a baseline (control) configuration with constant drag coefficients. The subsequent simulations are forced with NCEP reanalysis data from the first day of January 1979 to the last day of December 2010.

2.2. Parameterization of Atmospheric and Oceanic Drag Coefficients

Sea-ice motion is determined mainly by three forces: the internal stresses in the ice, the atmospheric drag force and the oceanic drag force (Steele et al., 1989). The momentum equations for the atmospheric drag $\boldsymbol{\tau}_a$ and the oceanic drag $\boldsymbol{\tau}_w$ are expressed through a quadratic drag relationship:

$$\boldsymbol{\tau}_a = \rho_a c_a |\boldsymbol{U}_a - \boldsymbol{u}| R_a (\boldsymbol{U}_a - \boldsymbol{u}) \,, \tag{1}$$

$$\boldsymbol{\tau}_w = \rho_w c_w |\boldsymbol{U}_w - \boldsymbol{u}| R_w (\boldsymbol{U}_w - \boldsymbol{u}) \,, \tag{2}$$

where ρ_a and ρ_w are the densities of air and sea water. The drag depends on the relative velocities $\boldsymbol{U}_{a,w} - \boldsymbol{u}$ where $\boldsymbol{U}_a$ is the atmospheric wind, $\boldsymbol{U}_w$ is the ocean current and $\boldsymbol{u}$ is the ice drift. The ocean (atmosphere) rotation matrix R_w (R_a) accounts for unresolved Ekman layers. c_a and c_w are the transfer coefficients for momentum, called air drag coefficient and water drag coefficient. From the Monin Obukhov similarity theory and a stability corrected logarithmic profile (Garbrecht et al., 2002) they can be expressed as:

$$c_D = \left[\frac{k}{ln\left(\frac{z_r}{z_0}\right) - \Psi_m\left(\frac{z_r}{L}\right)} \right]^2 \quad , \tag{3}$$

where $D = a$ for the atmosphere and $D = w$ for the ocean, z_r is a reference height (usually 10 m for the atmosphere, or the depth at which the current equals

geostrophic flow for the ocean, Lu et al., 2011), z_0 is the roughness length of sea ice, Ψ_m is the Dyer-Businger stability function, L the Monin Obukhov length, and k the von Karman constant. In case of neutral conditions, equation (3) reduces to the expression for the neutral drag coefficients:

$$c_{D,n} = \left[\frac{k}{ln\left(\frac{z_r}{z_0}\right)} \right]^2 \quad . \tag{4}$$

The roughness length z_0 changes regionally and temporally due to the presence and formation of topographic elements over/under the ice. Variability in z_0 implies variability in $c_{D,n}$. In this paper we focus on the neutral drag coefficients, that is, for the case of neutral stratification of the fluid (water and air). Thus, in the following the term drag coefficients always refer to neutral drag coefficients, except when stated otherwise.

In the baseline configuration, the sea ice-ocean model runs with constant neutral atmospheric and oceanic drag coefficients: $c_a = 1 \times 10^{-3}$ and $c_w = 5.4 \times 10^{-3}$, the latter value is chosen as the geostrophic drag coefficient proposed by McPhee (2008). These values correspond to a roughness length z_0 of $\approx 5 \times 10^{-5}$ m for the atmosphere-ice interface and $\approx 22 \times 10^{-3}$ m for the ocean-ice interface.

In order to arrive at drag coefficients that depend on sea-ice topography, we introduce the deformation energy R as a prognostic variable into the sea ice model. The deformation energy represents the sea-ice roughness and evolves in time (Steiner et al., 1999). Deformation energy changes with the work of internal forces in the ice E_{int} and with melting (Martin, 2007):

$$\frac{\partial R}{\partial t} = E_{int} + mRM - \nabla \cdot (\mathbf{u}R)\,, \tag{5}$$

where m is a constant (=1), and $\nabla \cdot (\mathbf{u}R)$ the change of R due to advection $(\mathbf{u} \cdot \nabla R)$ and convergence $R(\nabla \cdot \mathbf{u})$ of ice. M is the same melting rate that is used to thermodynamically change the ice volume, divided by the ice thickness. The term E_{int} is derived as the scalar product of the stress tensor $\boldsymbol{\sigma}$ and the

strain rate tensor $\dot{\boldsymbol{\varepsilon}}$ (Rothrock, 1975; Martin, 2007):

$$E_{int} = \boldsymbol{\sigma} \cdot \dot{\boldsymbol{\varepsilon}} = \sigma_I \varepsilon_I + \sigma_{II} \varepsilon_{II}, \tag{6}$$

where

$$\begin{aligned} \dot{\varepsilon}_I &= \dot{\varepsilon}_{11} + \dot{\varepsilon}_{22} \ , \\ \dot{\varepsilon}_{II} &= \sqrt{\left(\dot{\varepsilon}_{11} - \dot{\varepsilon}_{22}\right)^2 + 4\dot{\varepsilon}_{12}^2} \ , \end{aligned} \tag{7}$$

and

$$\begin{aligned} \sigma_I &= \tfrac{1}{2}\left(\sigma_{11} + \sigma_{22}\right), \\ \sigma_{II} &= \tfrac{1}{2}\sqrt{\left(\sigma_{11} - \sigma_{22}\right)^2 + 4\sigma_{12}^2} \end{aligned} \tag{8}$$

are invariants of the strain rate tensor $\dot{\boldsymbol{\varepsilon}}$ and of the stress tensor $\boldsymbol{\sigma}$ (Rothrock, 1975). This formulation for the deformation energy was previously implemented in uncoupled sea-ice models (Steiner et al., 1999; Martin, 2006, 2007).

It is important to note that not all of the energy spent during a deformation event is used to change the sea-ice topography which in turn has an impact on the momentum exchange. The total deformation work performed on an ice cover is transformed into potential energy stored in pressure ridges, into plastic deformation and into work due to friction. Thus, a limitation of the present parameterization is the requirement to quantify how much of the energy is actually spent to build up ridges and other topographic elements, but this is difficult to estimate (see Steiner et al., 1999, and references herein).

Drag coefficients depend on both surface roughness and stratification of the surface layers of the ocean or atmosphere. The NCEP Climate Forecast System reanalysis that we use here (Saha et al., 2014) already includes a stability parameterization to account for the differences in fluxes between the ice surface and the adjacent atmosphere as function of wind speed and static stability of the surface layer. Thus, we choose a parameterization that focuses only on the dependence on the surface roughness. Many studies focusing on the dependency of neutral drag coefficients on surface roughness (e.g. Garbrecht et al.,

1999, 2002; Lüpkes et al., 2012, 2013; Lüpkes & Gryanik, 2015) are based on the the partitioning approach by Arya (1973, 1975). According to this approach, the neutral drag coefficient is given as the sum of a skin drag, accounting for small-scale roughness, and a form drag, accounting for the influence of large obstacles (due to pressure difference before and behind the obstacle). This can be written as:

$$c_D = c_D^{\text{skin}} + c_D^{\text{form}} \qquad . \tag{9}$$

The form drag is usually expressed based on geometric consideration of the obstacles such as ridges (Garbrecht et al., 1999, 2002), melt ponds and ice floes (Lüpkes et al., 2012, 2013; Lüpkes & Gryanik, 2015). Following Steiner (2001), the neutral drag coefficients are expressed as a function of deformation energy R and ice concentration A:

$$c_a\left(R, A\right) = b_a + m_a R + d_a \left[1 - 4\left(A - \frac{1}{2}\right)^2\right] , \tag{10}$$

$$c_w\left(R, A\right) = b_w + m_w R + d_w \left[1 - 4\left(A - \frac{1}{2}\right)^2\right] . \tag{11}$$

The skin drag (the terms b_a and b_w in equations (10) and (11)) accounts for small scale roughness and it is chosen following Steiner (2001) according to the lowest observed drag coefficients: $b_a = 0.8 \times 10^{-3}$ and $b_w = 1.2 \times 10^{-3}$ (see e.g. Shirasawa & Aota, 1991; Shirasawa & Ingram, 1991; Wamser & Martinson, 1993). The form drag accounts for large scale obstacles and it is parameterized as a function of deformation energy R (second term on the right hand side of equations (10) and (11)) and of ice concentration (third term on the right hand side of equations (10) and (11)). According to equations (10) and (11), the drag coefficients increase linearly with the deformation energy and depend quadratically on ice concentration with a maximum of d_a (d_w) at $A = 0.5$ (50% ice concentration, see also Figure 1 in Steiner, 2001). Initially, the values of the parameters m_a, m_w, d_a and d_w are set to the values optimized via comparison with observed buoy-drift velocities (Steiner, 2001, see also Table 2). In Section

2.3, they are optimized by performing a sensitivity analysis based on comparison with sea-ice observations.

Note, that in this configuration the deformation energy does not affect the sea ice or the ocean directly because the sea-ice model does not employ a dynamic ice thickness distribution (as in, e.g., Ungermann et al., 2017). This means that we do not redistribute the ice between thickness categories according to variations of deformation energy. The only feedback on the physics of the model is through the atmospheric and oceanic drag coefficients that enter the momentum equation of the sea ice and of the ocean.

2.3. Choice of parameters

Equations (10) and (11) contain 6 parameters: b_a, b_w, m_a, m_w, d_a and d_w. The skin drags b_a and b_w are directly constrained by observations (e.g. Shirasawa & Aota, 1991; Shirasawa & Ingram, 1991; Wamser & Martinson, 1993). In order to find the best set of parameter values for m_a, m_w, d_a and d_w, we compare the model results with observations in a sensitivity study. To evaluate our model results quantitatively we use a cost function from satellite observations as a measure for model quality (Ungermann et al., 2017). In a second step, we use a Greens functions approach to obtain a set of optimal parameters (for details see Menemenlis et al., 2005; Ungermann et al., 2017). The construction of the cost function follows Kauker et al. (2015) and it is described in details in Ungermann et al. (2017). We use four different datasets: 1) the reprocessed concentration dataset from OSISAF EUM ([Online]) and its error estimates (1979 - 2009); (2) the ICESat-JPL thickness product (Kwok & Cunningham, 2008) with a local error estimated as in Kauker et al. (2015) yet with an upper limit of 1 m for the uncertainty (March as well as October/November, 2003 - 2008); (3) the OSISAF winter sea ice drift (Lavergne et al., 2010, October to April, 2002 - 2006) and (4) the summer sea ice drift from Kimura et al. (2013) (May to July, 2003 - 2007), which both use passive-microwave satellite data, with error estimates of Sumata et al. (2014, 2015). For ice concentration and ice thickness we compute the cost function separately for winter and for summer.

We focused the sensitivity study on the parameters m_a, m_w, d_a and d_w. In Table 2 we list the values of the original parameters and the final values after two optimization cycles. In this study we compare three different model runs: DRAGS, using the optimized parameters to compute variable drag coefficients; MEAN, using constant drag coefficients (to keep the Nansen number $\mathrm{Na} = \sqrt{\rho_a c_a / \rho_w c_w}$ comparable we use the mean values from DRAGS as constant drag coefficients, see Table 3); and CTRL using constant drag coefficients with the original values (Castro-Morales et al., 2014). The cost function values of these configurations are given in Table 4.

3. Results

In this section we present results for climatologies obtained from the first day of January 1990 to the last day of December 2010. The first ten years (1979-1989) of the simulations are not used because during this time the model adapts to the new forcing and to the new physics. We focus our analysis on the months of March (maximum sea-ice extent) and September (minimum sea-ice extent).

The model domain with the following regions is shown in Figure 1: Lincoln Sea (LS), Central Arctic (AC), Beaufort Sea (BS), East Siberian Sea (ESS), and Laptev Sea (LapS).

3.1. Simulated Deformation Energy and Drag Coefficients

Values for deformation energy in the Arctic basin vary between 20 and $300\,\mathrm{kJ/m^2}$ (Figure 2). Lower values are found towards the Marginal sea Ice Zone (MIZ) whereas values higher than $300\,\mathrm{kJ/m^2}$ characterize the coastal areas along the north coast of Greenland and the north coasts of the Arctic Canadian Archipelago, where ice is usually pushed against land and thus more deformed. In the Central Arctic the values vary between 25 and $95\,\mathrm{kJ/m^2}$, in agreement with Steiner et al. (1999).

The distribution of drag coefficient values is governed by the linear dependence on the deformation energy (equations (10) and (11)). The impact of ice

concentration is only visible where A<1 (not shown). Simulated atmospheric and oceanic drag coefficients are higher in summer than in winter (Table 5). Maximum values of both atmospheric and oceanic drag coefficients are found in the Lincoln Sea, minimum values in the Laptev Sea. Oceanic drag coefficients show a larger variability (due to larger values of m_w and d_w compared to m_a and d_a in equations (10) and (11)) in both summer and winter.

Changes in drag coefficients reflect changes in the roughness length z_0 (Section 2.2). In order to calculate the roughness length for the atmosphere, that is for the upper sea-ice surface, and for the ocean, that is for the surface underneath the ice, we use equation (4) with 10 m as reference height for the atmosphere and 5 m for the ocean as in Shaw et al. (2008). Values of surface roughness length vary between 0.7×10^{-5} m and 0.027 m (Figure 3a-b). These results compare well with the values of roughness length for different ice classes in Guest & Davidson (1991). In particular, the maximum value of 0.027 m is the same as the value of 0.027 m for very rough ice in Guest & Davidson (1991). The mean value in the Lincoln Sea (Table 6) agrees with the value of 2.0×10^{-3} for smooth MYI, whereas the mean values in BS, CA, ESS and LapS (Table 6) agree with the values for very smooth and smooth FYI (Guest & Davidson, 1991). Values for the under-ice roughness length varying from 0.05×10^{-3} m to 0.16 m (Figure 3c-d) are also in agreement with observations (Shaw et al., 2008).

3.2. Contributions to atmospheric and oceanic drag coefficients

To analyze the causes of the regional and seasonal differences in atmospheric and oceanic drag coefficients, we look at the contribution in equations (10) and (11) of the terms due to deformation energy and ice concentration as ratios between skin drag, deformation energy term and ice concentration term over the total atmospheric drag coefficients (Figure 4), and oceanic drag coefficients (not shown). In winter, the skin drag dominates both atmospheric and oceanic drag coefficients, mainly in the Eastern sector of the Arctic Ocean. In summer, the skin drag dominates in the MIZ, where the deformation energy is low and

the ice concentration is lower than 0.5. The deformation energy term dominates in the Western sector of the Arctic Ocean and its contribution is generally higher in winter. The contribution of the ice concentration term in winter is negligible almost everywhere in the Arctic Basin, except for the MIZ, which in winter extends to the Barent Sea and south of the Svalbard Islands. In summer, its contribution increases everywhere in the Arctic Ocean with maxima in the Laptev Sea of up to 80% of the total drag coefficient values.

To analyze in more detail the contribution of deformation and ice concentration in the computation of the atmospheric drag coefficients, we show in Figure 5 the time evolution (from 1990 to 2010) of mean atmospheric drag coefficients due to deformation energy and due to ice concentration in some regions of interest. In general, the contribution due to ice concentration shows a larger seasonal variability since in winter the ice concentration approaches 1 almost everywhere in the Arctic and the ice concentration term drops to zero. The contribution of the two terms is different for different regions, and shows also an interannual variability. In the Lincoln Sea, the total atmospheric drag is always dominated by deformation. In the Central Arctic, the deformation energy term dominates in winter, whereas in summer the drag is dominated by the ice concentration term. In the Laptev Sea (not shown) the contribution of the deformation energy remains always very small. In the Beaufort Sea the contribution of the two terms varies with time, the same holds for the East Siberian Sea (not shown).

3.3. Sea Ice

Mean summer ice concentration is lowest in the Laptev Sea and East Siberian Sea ($A < 0.4$) and highest in the Lincoln Sea and the Central Arctic ($A > 0.8$) in both DRAGS and MEAN (Table 7). In winter, the differences between the two runs (DRAGS-MEAN) in ice concentration are visible only in the MIZ (Figure 6a). In summer, the ice concentration is reduced almost everywhere in the Arctic basin when we introduce variable drag coefficients (DRAGS), except for the Beaufort Sea (Figure 6b). Nevertheless, in both winter and summer the differences are very low (between 10% and 20%).

Mean summer ice thickness in the Arctic Ocean ranges from 0.5 m in the East Siberian Sea and Laptev Sea to up to 7 m in the Lincoln Sea (Table 7). Between DRAGS and MEAN the ice thickness shows differences, very similar in March and September, in the western sector of the Arctic Ocean. Except for the Lincoln Sea, where differences are even larger than 1 m, these differences remain on the order of 0.5 m. Due to the large variability in ice thickness values, also in the Lincoln Sea differences are not larger than one standard deviation.

In our simulations, summer sea ice velocities are on the order of 5 cm s^{-1} in the Arctic Ocean. Amongst the different regions, faster ice is a characteristic of the Beaufort Sea with 5.25 cm s^{-1} in DRAGS and 4.90 cm s^{-1} in MEAN. Very low values are found in the Lincoln Sea where the ice remains constrained between the coasts of Greenland and Ellesmere Island and it is characterized by velocities smaller than 1 cm s^{-1}. North of Greenland and in the Fram Strait the ice moves faster in DRAGS than in MEAN and the arrows indicate a larger export of ice through the Fram Strait. In summer, when the ice is more mobile, differences are larger and the pattern of these differences is more pronounced. The drift difference arrows show the cyclonic pattern in the Beaufort Gyre (Figure 6f) that usually dominates in summer, thus showing an increased cyclonic circulation in DRAGS than in MEAN. Only in the Lincoln Sea differences in mean drift are larger than one standard deviation from the mean drift in MEAN.

3.4. Ocean Surface

In order to evaluate the effects of the new drag formulation on the surface ocean, we analyze sea surface temperature θ, surface salinity and Mixed Layer Depth (MLD).

In winter, temperatures are equal to the freezing point everywhere in the Arctic Ocean, except in the MIZ (Figure 7 and Table 7). From Figure 7 the coldest summer temperatures are found in the Nansen Basin and the warmest temperatures in the MIZ. Mean values vary between $-0.24\,^{\circ}$C in the East-Siberian Sea and $-1.66\,^{\circ}$C in the Lincoln Sea. Temperature differences between DRAGS and MEANS are no larger than $0.06\,^{\circ}$C. Only in the Lincoln Sea, the

mean sea surface temperature in DRAGS differs from the mean value in MEAN by more than one standard deviation.

Surface salinity in winter ranges between 33 and 35 except for the Beaufort Sea and East-Siberian Sea, where values are lower than 32 (Figure 8a). The surface salinity differences in winter are generally small (order of 0.2). Only in the Laptev Sea and Kara Sea the DRAGS surface salinity are lower by 0.5 than in the MEAN run. In summer, the ocean surface is more saline everywhere in the DRAGS run.

On average, the mean MLD in September is deeper by 3 m in the DRAGS run than in the MEAN run (Fig 10a, c). This is a big difference because in the MEAN run, the MLD reaches average summer depths in the sea ice covered area of 8 m±2 m. In winter, the mixed layer is deeper everywhere in the Arctic Basin for both MEAN (39±11ṁ) and DRAGS (43±12 m). The differences DRAGS - MEAN in winter MLD are smaller than in summer. Note that the model layer thickness is 10 m at the surface. We use a density criterion (Section 2) to estimate MLDs from the vertical density gradient. The effects of variable surface ocean stress on the MLD should be tested using an ocean model that can resolve the ocean surface at a finer scale (1-3 m). In this case, though, the approach used in the present work, i.e. using the computed drag coefficients to calculate the ocean currents in the first surface layer, would result erroneous (Roy et al., 2015).

3.5. Ocean Interior

We evaluate the effects of the new drag parameterization on the ocean interior by analyzing the September stream function, a vertical salinity profile along an oceanic transect through a large freshwater reservoir in the Beaufort Sea in September (Figure 1), and the circulation in the mid Atlantic Water (mid-AW) layer between 350 m and 800 m depth.

The stream function (Figure 9) illustrates the well-known Arctic circulation pattern with a more or less clear separation between the Eurasian and Canadian Basin (Steiner et al., 2004). There is a strong surface anticyclonic circulation in

the Beaufort Sea, whereas the Central Arctic ocean circulation is dominated by a cyclonic pattern of the Atlantic water in the ocean interior. The differences DRAGS - MEAN (Figure 9d) point to a stronger Beaufort Gyre in DRAGS in agreement with the ice drift: stronger ice drift leads to an intensified anticyclonic circulation also in the upper ocean layer. The cyclonic pattern in the central Arctic Ocean interior is also stronger.

The vertical salinity profile (Figure 10a) down to 250 m for the DRAGS run shows the accumulation of fresher water at the surface of the Beaufort Sea. The 32 isohaline reaches down to ca. 150 m. The difference map DRAGS - MEAN (Figure 10b) shows a thin layer of saltier water at the surface (first 10 meters) in agreement with Figure 8d. In the deep Beaufort sea, the difference map shows fresher water extending to $\sim$120 m depth. In the Central Arctic (CA) the DRAGS run water masses are saltier, with differences extending down to $\sim$250 m depth.

Finally, we compare the circulation of the Atlantic water in the mid-AW layer. In Figure 11a we show the mid-AW circulation in the DRAGS run. The typical pattern as inferred from observations (Carmack et al., 1995; Rudels et al., 1994, 1999; Swift et al., 1997) and previous model results (Holland et al., 1996; Karcher & Oberhuber, 2002; Karcher et al., 2003) is represented. The circulation is cyclonic in the Beaufort Sea-Canadian Basin and in the Makarov Basin. The inflow from the Fram Strait with a branch of mid-AW flowing along the continental margins of the Eurasian and Makarov Basin is also represented. Finally, a branch of mid-AW separates from the Alpha Ridge and flows along the continental slope of Greenland to exit through the Fram Strait. The cyclonic circulation in the Beaufort Sea is slightly slower in the DRAGS run (Figure 11b). A stronger flow of mid-AW between the Alpha Ridge and Makarov Basin is directed towards the Fram Strait. Also the flow along the Lincoln Shelf is enhanced. In the Makarov Basin the cyclonic mid-AW circulation is slowed down for DRAGS compared to MEAN. The differences are never larger than one standard deviation from the velocities in the MEAN run.

3.6. Differences between new mean drag coefficients and original values

The newly implemented drag coefficients parameterization not only leads to more variability, but also to mean drag coefficients that are generally larger (atmosphere) or smaller (ocean) than the default values of CTRL. This implies a change in the Nansen number between MEAN and CTRL that can lead to changes in sea-ice drift and sea-ice properties. In particular, we expect faster ice as a result of the higher atmospheric drag coefficients (1.36×10^{-3} compared to 1×10^{-3}) and the lower oceanic ones (2.82×10^{-3} compared to 5.4×10^{-3}). This motivates an additional comparison for the simulated sea-ice properties between the MEAN run and the CTRL run. Mean values of sea-ice concentration, thickness and drift for the entire Arctic Basin and for regions of interested are listed in Table 7. Difference map for sea-ice concentration, thickness and drift in March and September are shown in Figure 12.

Differences in ice concentration are larger in September than in March. During winter, the ice concentration is 1 almost everywhere in the Arctic Ocean, so differences are seen only in the MIZ (Figure 12a). In summer, the sea-ice areal extent in MEAN is reduced in the Central Arctic Basin, Lincoln Sea and Beaufort Sea (Table 7). A stronger reduction is seen in the East Siberian Sea, Laptev Sea and Kara Sea. Ice thickness (Figure 12c and d) is reduced in large parts of the Arctic Basin in winter, with the exception of the Chukchi Sea where the ice thickness in MEAN is ~ 0.5 m larger than in CTRL. In summer, the pattern is the same, with a general reduction of ice over the entire Arctic Ocean. Large differences are seen in the Lincoln Sea with mean summer ice thickness decreasing from 8.46 m in CTRL to 7.86 m in MEAN. The ice moves faster in MEAN than in CTRL, as expected by the change in the Nansen number. Particularly, the circulation patters are enhanced in both winter and summer. Figures 12e and f show a stronger Beaufort Gyre, and a stronger transpolar drift stream. Differences are relevant in the Lincoln Sea with changes in mean summer drift from $0.02\,\mathrm{cm\,s^{-1}}$ in CTRL to $0.11\,\mathrm{cm\,s^{-1}}$ in MEAN, and in the Central Arctic with an increase from $1.58\,\mathrm{cm\,s^{-1}}$ in CTRL to $2.43\,\mathrm{cm\,s^{-1}}$ in MEAN.

4. Discussion

With the implementation of equations (10) and (11), drag coefficients vary according to season and region: Between 0.88 $\times 10^{-3}$ and 4.68 $\times 10^{-3}$ for atmospheric drag coefficients, and between 1.28 $\times 10^{-3}$ and 13.68 $\times 10^{-3}$ for the oceanic ones. Our computed atmospheric and oceanic drag coefficients fall into the range of observed and topography-based estimated values (see Table 3), but never reach the extremes. The Steiner (2001) approach relies on the fraction of energy that goes into deformation. This fraction is very difficult to constrain by measurements and represents a large uncertainty for the parameterization. For example, a too low fraction of energy used for deformation may lead to underestimating the term in the atmospheric and oceanic drag coefficient parameterization that depends linearly on ice deformation.

Our results for different regions represent the general pattern shown in large scale estimates based on satellite data (Petty et al., 2017) with higher values in regions where the ice is more deformed due to proximity to the coast (Lincoln Sea) and due to convergent drift (Central Arctic), and lower values in the marginal seas (Laptev Sea and East Siberian Sea). Note that each method of estimating drag coefficients is inaccurate because they all implicitly make different assumptions and employ different approximations and parameterizations.

Atmospheric drag coefficients computed in a different sea ice model (Tsamados et al., 2014) and based on different parameterizations than ours, vary between 2×10^{-3} and 4×10^{-3}, whereas oceanic drag coefficients vary between 3×10^{-3} and 9×10^{-3}, in good agreement with our results. Our results are very similar to those of Tsamados et al. (2014) in many respects: drag coefficients are higher in summer than in winter, and the contribution of the different terms differ with season, that is, in winter the total drag is dominated by deformation, whereas in summer the drag is dominated by the ice concentration term.

The newly implemented parameterization affects the simulated sea-ice properties, that is, extent, thickness and drift. In general, the ice is thinner and moves faster, and the overall area is reduced (Table 7). To compare the realism

of the different simulations, we use a cost function computed for the different sea ice variables in winter and in summer (Table 4). The total cost function value, that is, the model-data misfit is a little smaller for the DRAGS run than for the MEAN run. In particular, the ice concentration in both summer and winter, the summer ice thickness and the summer sea-ice drift are better simulated with the variable drag coefficients. The default values of constant drag coefficients in the CTRL run gives the largest model-data misfit (largest cost function), except for winter ice concentration. The differences DRAGS - CTRL in winter ice concentration (not shown) point to a southward shift of the marginal ice zone. This is due to the larger Nansen number in DRAGS that makes the ice more mobile. In winter, the atmospheric and oceanic drag coefficients in the MIZ are dominated by the ice concentration term (Figure 4) thus a proper tuning of the d_a and d_w parameters alone in equations (10) and (11) is required to decrease the misfit to observation in the winter MIZ.

In general, the differences between MEAN and CTRL are larger than between DRAGS and MEAN. We conclude that the variable drag parameterization improves the model simulation, but to first order, this improvement can already be achieved by adjusting the mean drag coefficients and hence the Nansen number. We can thus suggest a new set of constant drag coefficients that improve the simulated sea-ice characteristics. An independent optimization of constant drag coefficients (Nguyen et al., 2011) yielded different values, but in the present study the mean values emerge from the optimization of a more sophisticated drag coefficients parameterization. Additional improvement in the model simulations is caused by the spatial variability of the drag coefficients.

With variable drag coefficients in the DRAGS run mixing tends to be stronger leading to deeper mixed layers. MLDs estimates from observations are sparse. In summer, the few available ones range from 8 m to 20 m in the Beaufort Sea (Yang et al., 2004; Lemke & Manley, 1984; Peralta-Ferriz & Woodgate, 2015). The mean MLD of 10 m in the DRAGS run agrees better with these estimates than the 7 m in the MEAN run. MLD data based on the NOAA World Ocean Atlas (Monterey & deWitt, 1997) give a mean value of 8.7 m (and values up to

440 m) for the entire Arctic Basin in September. Here, the mean MLD of 8±2 m in the MEAN run appears to be closer to observation than the mean of 11±2 m in the DRAGS run, but this is confounded by the large range of MLDs in the observations and the ambiguous estimation methods. In winter in the Central Arctic, MLD values are between 25 m and 50 m (Treshnikov & Baranov, 1973), compared to the simulated 42 m in both MEAN and DRAGS. In general, the agreement with independent estimates of MLDs is ambiguous and both DRAGS and MEAN agree with observational estimates similarly well. We remind that our numerical surface ocean layer is 10 m thick and MLDs are sometimes smaller making our MLD estimates less accurate than with a model with higher vertical resolution.

Changes due to variable drag coefficients in sea surface temperatures are small in most regions. Note that in the present model study the heat exchange coefficients do not depend on the surface roughness, thus the changes in surface temperature are only an indirect consequence of the changes in the sea-ice properties. Differences in salinity point to a more saline sea surface in summer and fresher water in the interior of the Beaufort Sea. The amount of fresh water relative to a reference salinity of 34.8 (Proshutinsky et al., 2009; Roy et al., 2015) in the Beaufort Sea (not shown here) is larger in DRAGS than in MEAN. This agrees with Roy et al. (2015) who show an increased fresh water retention in the Beaufort Gyre due to stronger ice-ocean and air-ice roughness. The mean values of atmospheric and oceanic drag coefficients in the Beaufort Sea (see Table 5) point to a larger surface and bottom-surface roughness in this region compared to the values in MEAN. On the other hand, the fresh water of CTRL is lower than in MEAN implying that the difference are mainly driven by the increase in air-ice roughness in MEAN. The total liquid Arctic fresh water budget is higher in MEAN than in the DRAGS and in the CTRL runs, but the differences remain very small.

5. Summary and Conclusion

Atmospheric and oceanic drag coefficients vary in time and space as a consequence of the interplay between sea-ice deformation and sea-ice concentration. In the present study, we introduce variable atmospheric and oceanic drag coefficients in a coupled sea-ice–ocean model and we quantify the effects of the new parameterization on the main sea-ice properties and on the ocean. This is achieved by comparing two simulations: a simulation with constant drag coefficients and a simulation where the drag coefficients are parameterized as a function of ice concentration and deformation energy.

Simulated atmospheric and oceanic drag coefficients fall in the range of observed values and agree with recent estimates based on topography profiles and model results. In our study resulting atmospheric and oceanic drag coefficients can evolve spatially and temporally as function of sea-ice characteristics: In winter, drag coefficients are dominated by sea-ice deformation, whereas in summer ice concentration contributes most.

The dynamic sea-ice state is affected by the new parameterization. Particularly in summer, the ice is thinner, moves faster, and the areal extent is reduced when variable drag coefficients are used. The ice thickness shows differences up to 0.5 m in the Arctic basin and even larger than 1 m in the Lincoln Sea, pointing to a strong reduction of ice volume in that region. The variable drag parameterization does not have a uniform effect in the Arctic basin, but the impact is more visible in the western sector of the Arctic. With variable drag coefficients the model misfit with observations is improved, particularly for sea-ice concentration in summer and winter, and sea-ice thickness and drift in summer. The mean values of drag coefficients computed from the run with variable ones are a better set of parameters for simulations with constant drag coefficients. The new set of constant drag coefficients is obtained by the optimization of a sophisticated drag coefficient parameterization and differ from values emerging by a different optimization.

Our study represents the first implementation of a parameterization for sur-

face dependent drag coefficients in a coupled sea ice-ocean model. Not only does this parameterization allow a more physical representation of the sea-ice evolution, but also it makes possible the analysis of its effects on the ocean circulation. With the new implementation, surface stresses are higher, and cause a deeper mixed layer, particularly in summer. The new computed mixed layer depths represent a slightly better agreement with observations in the Arctic in summer, particularly in the Beaufort Sea/Canada Basin. Finally the effects of the newly implemented parameterization reach the ocean interior causing changes in Atlantic water circulation. Based on the analysis of climatological maps these effects are small.

In a natural continuation of this study, the effect of our parameterization implementation on the atmosphere and ensuing feedbacks should be studied in a coupled atmosphere-ice-ocean model. Finally, in the light of the recent increase in sea-ice drift (Spreen et al., 2011; Kwok et al., 2013), our results may be even more relevant to the community.

Acknowledgments

We thank the CLIVAR (Climate and Ocean Variability, Predictability, and Change) working group for the release of CORE version 2, the NOAA's National Centers for Environmental Prediction (NCEP) for developing the NCEP-CFSv2 data set, and the Arctic Ocean Model Intercomparison Project (AOMIP, now FAMOS - Forum for Arctic Modeling & Observational Synthesis) for the release of the river runoff climatology. We would like to thank Michael Karcher, Frank Kauker, Hiroshi Sumata, and Kathrin Riemann-Campe, all affiliated with the Alfred Wegener Institute (AWI), for the interesting discussions that helped to understand and interpret the results.

References

([Online]). Ocean and Sea Ice Satellite Application Facility (2011), Global sea ice concentration reprocessing dataset 1978-2009 (v1.1). URL: `http://osisaf.`

met.no.

Andreas, E. L., Horst, T. W., Grachev, A. A., Persson, P. O. G., Fairall, C. W., Guest, P. S., & Jordan, R. E. (2010). Parametrizing turbulent exchange over summer sea ice and the marginal ice zone. *Q. J. R. Meteorol. Soc.*, *136(694)*, 927–943.

Arya, S. P. S. (1973). Contribution of form drag on pressure ridges to the air stress on Arctic ice. *J. Geophys. Res.*, *78(30)*, 7092–7099.

Arya, S. P. S. (1975). A drag partitioning theory for determining the large-scale roughness parameter and wind stress on the Arctic pack ice. *J. Geophys. Res.*, *80(24)*, 3447–3454.

Birnbaum, G., & Luepkes, C. (2002). A new parameterization of surface drag in the marginal sea ice zone. *Tellus*, *A, 54*, 107–123, doi: 10.1034/j.1600–0870.2002.00243.x.

Carmack, E. C., Macdonald, R. W., Perkin, R. G., McLaughlin, F. A., & Pearson, R. J. (1995). Evidence for warming of Atlantic water in the Southern Canadian Basin of the Arctic Ocean: Results from the Larsen-93 Expedition. *Geophys. Res. Lett.*, *22(9)*, 1061–1064, doi: 10.1029/95GL00808.

Castellani, G., Gerdes, R., Losch, M., & Lüpkes, C. (2015). Impact of Sea-Ice Bottom Topography on the Ekman Pumping. In G. Lohmann, H. Meggers, V. Unnithan, D. Wolf-Gladrow, J. Notholt, & A. Bracher (Eds.), *Towards an Interdisciplinary Approach in Earth System Science* Springer Earth System Sciences (pp. 139–148). Springer International Publishing. doi:10.1007/978-3-319-13865-7_16.

Castellani, G., Lüpkes, C., Hendricks, S., & Gerdes, R. (2014). Variability of Arctic sea ice topography and its impact on the atmospheric surface drag. *J. Geophys. Res. Oceans*, *119*, 6743–6762, doi:10.1002/2013JC009712.

Castro-Morales, K., Kauker, F., Losch, M., Hendricks, S., Riemann-Campe, K., & Gerdes, R. (2014). Sensitivity of simulated Arctic sea ice to realistic ice

thickness distributions and snow parameterizations. *J. Geophys. Res. Oceans*, *119*, 559–571, doi:10.1002/2013JC009342.

Curry, J. A., Schramm, J. L., & Ebert, E. E. (1995). Sea Ice-Albedo Climate Feedback Mechanism. *Journal of Climate*, *8*, 240–247.

Daru, V., & Tenaud, C. (2004). High order one-step monotonicity-preserving schemes for unsteady compressible flow calculations. *J. Comp. Phys.*, *193(2)*, 563–594, doi: 10.1016/j.jcp.2003.08.023.

Flocco, D., & Felthman, D. L. (2007). A continuum model of melt pond evolution on Arctic sea ice. *J. Geophys. Res. Oceans*, *112(C08016)*, doi:10.1029/2006JC003836.

Flocco, D., Felthman, D. L., & Turner, A. K. (2010). Incorporation of a physically based melt pond scheme into the sea ice component of a climate model. *J. Geophys. Res. Oceans*, *115(C08012)*, doi:10.1029/2009JC005568.

Garbrecht, T., Luepkes, C., Augstein, E., & Wamser, C. (1999). Influence of a sea ice ridge on low-level airflow. *J. Geophys. Res.*, *104*, 24,499–24,507.

Garbrecht, T., Lüpkes, C., Hartmann, J., & Wolff, M. (2002). Atmospheric drag coefficients over sea ice - validation of a parameterisation concept. *Tellus*, *A, 54*, 205–219, doi: 10.1034/j.1600–0870.2002.01253.x.

Guest, P., & Davidson, K. L. (1991). The aerodynamic roughness of different types of sea ice. *J. Geophys. Res. Oceans*, *96(C3)*, 4709–4721, doi:10.1029/90JC02261.

Haas, C., Pfaffling, A., Hendricks, S., Rabenstein, L., Etienne, J.-L., & Rigor, I. (2008). Reduced ice thickness in Arctic Transpolar Drift favors rapid ice retreat. *Geophys. Res. Lett.*, *35(L17501)*, doi:10.1029/2008GL034457.

Hibler, W. D. (1979). A dynamic thermodynamic sea ice model. *J. Phys. Oceanogr.*, *9*, 815–846.

Hibler, W. D. (1980). Modeling a variable thickness sea ice cover. *Mon. Weather Rev.*, *108*, 1943–1973.

Hibler, W. D. (1984). The role of sea ice dynamics in modeling CO_2 increases. In J. E. Hansen, & T. Takahashi (Eds.), *Climate Processes and Climate sensitivity*. AGU, Washington, D. C., doi: 10.1029/GM029p0238.

Holland, D. M., Mysak, L. A., & Oberhuber, J. M. (1996). An investigation of the general circulation of the Arctic Ocean using an isopycnal model. *Tellus*, *A, 48*, 138–157. doi: 10.1034/j.1600–0870.1996.00008.x.

Hunke, E. (2010). Thickness sensitivities in the CICE sea ice model. *Ocean Mod.*, *34*, 137–149, doi:10.1016/j.ocemod.2010.05.004.

Hunke, E. C., Lipscomb, W. H., & Turner, A. K. (2010). Sea-ice model for climate study: retrospective and new directions. *J. Glaciol.*, *56*, 1162–1172.

Hunke, E. C., Lipscomb, W. H., Turner, A. K., Jeffery, N., & Elliott, S. (2015). CICE: the Los Alamos Sea Ice Model Documentation and Software User's Manual. Version 5.1, LA-CC-06-012, . *Los Alamos Natl. Lab., Los Alamos, N. M.*.

Kara, A. B., Rochford, P. A., & Hurlburt, H. E. (2000). An optimal definition for ocean mixed layer depth. *Journal of Geophysical Research: Oceans*, *105*, 16803–16821. doi:10.1029/2000JC900072.

Karcher, M., Beszcynska-Moeller, A., Kauker, F., Gerdes, R., Heyden, S., Rudels, B., & Schauer, U. (2011). Arctic Ocean warming and its consequences for the Denmark Strait overflow. *J. Geophys. Res.*, *116(C02037)*, doi:10.1029/2010JC006265.

Karcher, M., Gerdes, R., Kauker, F., & Köberle, C. (2003). Arctic warming: Evolution and spreading of the 1990s warm event in the Nordic Seas and the Arctic Ocean. *J. Geophys. Res.*, *108, 3034*, doi:10.1029/2001JC001265, C2.

Karcher, M., & Oberhuber, J. M. (2002). Pathways and modification of the upper and intermediate water of the Arctic Ocean. *J. Geophys. Res.*, *107(C6)*, doi: 10.1029/2000JC000530.

Kauker, F., Kaminski, T., Ricker, R., Toudal-Pedersen, L., Dybkjaer, G., Melsheimer, C., Eastwood, S., Sumata, H., Karcher, M., & Gerdes, R. (2015). Seasonal sea ice predictions for the Arctic based on assimilation of remotely sensed observations. *The Cryosphere Discussion*, *9*, 5521–5554.

Kimura, N., Nishimura, A., Tanaka, Y., & Yamaguchi, H. (2013). Influence of winter sea-ice motion on summer ice cover in the Arctic. *Polar Research*, *32*.

Kwok, R., & Cunningham, G. F. (2008). ICESat over Arctic sea ice: Estimation of snow depth and ice thickness. *J. Geophys. Res. Oceans*, *113*. doi:10.1029/2008JC004753. C08010.

Kwok, R., Spreen, G., & Pang, S. (2013). Arctic sea ice circulation and drift speed: Decadal trends and ocean currents. *J. Geophys. Res. Oceans*, *118*, 2408–2425, doi:10.1002/jgrc.20191.

Large, W. G., McWilliams, J. C., & Doney, S. C. (1994). Ocean vertical mixing: A review and a model with a nonlocal boundary layer parameterization. *Rev. Geophys.*, *32(4)*, 363–403, doi:10.1029/94RG01872.

Large, W. G., & Yeager, S. G. (2009). The global climatology of an interannually varying air–sea flux data set. *Climate Dynamics*, *33*, 341–364. doi:10.1007/s00382-008-0441-3.

Lavergne, T., Eastwood, S., Teffah, Z., Schyberg, H., & Breivik, L.-A. (2010). Sea ice motion from low-resolution satellite sensors: An alternative method and its validation in the Arctic. *J. Geophys. Res. Oceans*, *115*. doi:10.1029/2009JC005958. C10032.

Laxon, S. W., Giles, K. A., Ridout, A. L., Wingham, D. J., Willatt, R., Cullen, R., Kwok, R., Schweiger, A., Zhang, J., Haas, C., Hendricks, S., Krishfield,

R., Kurtz, N., Farrell, S., & Davidson, M. (2013). CryoSat-2 estimates of Arctic sea ice thickness and volume. *Geophys. Res. Lett.*, *40*, 732–737, doi:10.1002/grl.50193.

Lemke, P., & Manley, T. O. (1984). The seasonal variation of the mixed layer and the pycnocline under polar sea ice. *J. Geophys. Res. Oceans*, *89*, 6494–6504. doi:10.1029/JC089iC04p06494.

Losch, M., Menemenlis, D., Campin, J. M., Heimbach, P., & Hill, C. (2010). On the formulation of sea-ice models: Part 1: Effects of different solver implementations and parameterizations. *Ocean Mod.*, *33*, 129–144, doi: 10.1016/j.ocemod.2009.12.008.

Lu, P., Li, Z., Cheng, B., & Leppäranta, M. (2011). A parameterization of the ice-ocean drag coefficient. *J. Geophys. Res.*, *116, C07019*, doi:10.1029/2010C006878.

Lüpkes, C., & Birnbaum, G. (2005). Surface drag in the Arctic marginal sea-ice zone: A comparison of different parameterisation concepts. *Boundary-Layer Meteorology*, *117*, 179–211, doi: 10.1007/s10546–005–1445–8.

Lüpkes, C., & Gryanik, V. M. (2015). A stability-dependent parametrization of transfer coefficients for momentum and heat over polar sea ice to be used in climate models. *J. Geophys. Res. Atmospheres*, *120*, 552–581. doi:10.1002/2014JD022418.

Lüpkes, C., Gryanik, V. M., Hartmann, J., & Andreas, E. L. (2012). A parametrization, based on sea ice morphology, of the neutral atmospheric drag coefficients for weather prediction and climate models. *J. Geophys. Res.*, *117, D13112*, doi: 10.1029/2012JD017630.

Lüpkes, C., Gryanik, V. M., Roesel, V. M., Birnbaum, G., & Kaleschke, L. (2013). Effect of sea ice morphology during Arctic summer on atmospheric drag coefficients used in climate models. *Geophys. Res. Lett.*, *40(2)*, 446–451, doi:10.1002/grl.50081.

Marshall, J., Adcroft, A. J., Hill, C. N., Perelman, L., & Heisey, C. (1997). A finite-volume, incompressible Navier Stokes model for studies of the ocean on parallel computers. *J. Geophys. Res.*, *102(C3)*, 5753–5766, doi:10.1029/96JC02775.

Martin, T. (2006). Comparison of different ridge formation models of Arctic sea ice with observations from laser profiling. *Ann. Glaciol.*, *44*, 403–410.

Martin, T. (2007). *Arctic Sea Ice Dynamics: Drift and Ridging in Numerical Models and Observations*. Ph.D. thesis Bremen University. Berichte zur Polar- und Meeresforschung (Reports on Polar and Marine Research), Bremerhaven, Alfred Wegener Institute for Polar and Marine Research, 563, 229 p.

Martin, T., Steele, M., & Zhang, J. (2014). Seasonality and long-term trend of Arctic Ocean surface stress in a model. *Journal of Geophysical Research: Oceans*, *119*, 1723–1738. doi:10.1002/2013JC009425.

Martin, T., Tsamados, M., Schroeder, D., & Feltham, D. L. (2016). The impact of variable sea ice roughness on changes in Arctic Ocean surface stress: A model study. *J. Geophys. Res. Oceans*, *121*, 1931–1952. doi:10.1002/2015JC011186.

McPhee, M. G. (2008). *Air-Ice-Ocean Interaction: Turbulent Ocean Boundary Layer Exchange Processes*. Springer, Miles McPhee Research Company, Naches, Wash.

Menemenlis, D., Fukumori, I., & Lee, T. (2005). Using Green's Functions to Calibrate an Ocean General Circulation Model. *Monthly Weather Review*, *133*, 1224–1240. doi:10.1175/MWR2912.1.

Monterey, G., & deWitt, L. (1997). Seasonal variability of global mixed layer depth from WOD98 temperature and salinity profiles. *NOAA Atlas NESDIS*, *14*, 964–978. doi: 10.1034/j.1600–0870.1999.00029.x.

Nguyen, A. T., Menemenlis, D., & Kwok, R. (2011). Arctic ice-ocean simulation with optimized model parameters: Approach and assessment. *Journal of Geophysical Research: Oceans*, *116(C04025)*. doi:10.1029/2010JC006573.

Peralta-Ferriz, C., & Woodgate, R. A. (2015). Seasonal and interannual variability of pan-Arctic surface mixed layer properties from 1979 to 2012 from hydrographic data, and the dominance of stratification for multi-year mixed layer depth shoaling. *Progress in Oceanography*, *134*, 19–53, doi:10.1016/j.pocean.2014.12.005.

Petty, A. A., Tsamados, M. C., & Kurtz, N. T. (2017). Atmospheric form drag coefficients over Arctic sea ice using remotely sensed ice topography data, spring 2009–2015. *J. Geophys. Res. Earth Surface*, *122*, 1472–1490. doi:10.1002/2017JF004209.

Proshutinsky, A., Krishfield, R., Timmermans, M.-L., Toole, J., Carmack, E., McLaughlin, F., Williams, W. J., Zimmermann, S., Itoh, M., & Shimada, K. (2009). Beaufort Gyre freshwater reservoir: State and variability from observations. *Journal of Geophysical Research: Oceans*, *114*. doi:10.1029/2008JC005104.

Proshutinsky, A., Steele, M., Zhang, J., Holloway, G., Steiner, N., Häkkinen, S., Holland, D. M., Gerdes, R., Köberle, C., Karcher, M., Johnson, M., Maslowsky, W., Zhang, Y., Hibler, W. D., & Wang, J. (2001). The Arctic Ocean Model Intercomparison Project (AOMIP). *EOS*, *82(51)*, 637–644.

Rabenstein, L., Hendricks, S., Martin, T., Pfaffhuber, A., & Haas, C. (2010). Thickness and surface-properties of different sea-ice regimes within the Arctic Trans Polar Drift: Data from summers 2001, 2004 and 2007. *J. Geophys. Res.*, *115, C12059*, doi:10.1029/2009JC005846.

Rothrock, D. A. (1975). The Energetics of the Plastic Deformation of Pack Ice by Ridging. *J. Geophys. Res.*, *80(33)*, 4514–4519, doi:10.1029/JC080i033p04514.

Rothrock, D. A., Yu, Y., & Maykut, G. A. (1999). Thinning of Arctic sea-ice cover. *Geophys. Res. Lett.*, *26(23)*, 3469–3472, doi: 10.1029/1999GL010863.

Roy, F., Chevallier, M., Smith, G. C., Dupont, F., Garric, G., Lemieux, J.-F., Lu, Y., & Davidson, F. (2015). Arctic sea ice and freshwater sensitivity to the treatment of the atmosphere-ice-ocean surface layer. *J. Geophys. Res. Oceans*, *120*, 4392–4417, doi:10.1002/ 2014JC010677.

Rudels, B., Friedrich, H. J., & Quadfasel, D. (1999). The Arctic Circumpolar Boundary Current. *Deep-Sea Res. Part II: Topical Studies in Oceanography*, *46*, 1023–1062.

Rudels, B., Jones, E. P., Anderson, L. G., & Kattner, G. (1994). On the intermediate Depth Waters of the Arctic Ocean. In O. M. Johannessen, R. D. Muench, & J. E. Overland (Eds.), *The Polar Oceans and Their Role in shaping the Global Climate: The Nansen Centennial Volume* (pp. 33–46). Washington: American Geophysical Union.

Saha, S., Moorthi, S., Wu, X., Wang, J., Nadiga, S., Tripp, P., Behringer, D., Hou, Y.-T., Chuang, H.-y., Iredell, M., Ek, M., Meng, J., Yang, R., Mendez, M. P., van den Dool, H., Zhang, Q., Wang, W., Chen, M., & Becker, E. (2014). The NCEP Climate Forecast System Version 2. *Journal of Climate*, *27*, 2185–2208. doi:10.1175/JCLI-D-12-00823.1.

Semtner, A. J. (1976). A Model for the Thermodynamic Growth of Sea Ice in Numerical Investigations of Climate. *Journal of Physical Oceanography*, *6*, 379–389. doi:10.1175/1520-0485(1976)006<0379:AMFTTG>2.0.CO;2.

Serreze, M. C., Holland, M. M., & Stroeve, J. (2007). Perspectives on the Arctic's Shrinking Sea-Ice Cover. *Science*, *315(5818)*, 1533–1536, doi: 10.1126/science.1139426.

Serreze, M. C., Maslanik, J. A., Scambos, T. A., Fetterer, F., Stroeve, J., Knowles, K., Fowler, C., Drobot, S., Barry, R. G., & Haran, T. M. (2003). A

record minimum Arctic sea ice extent and area in 2002. *Geophys. Res. Lett.*, *30(1110)*, doi:10.1029/2002GL016406.

Shaw, W. J., Stanton, T. P., McPhee, M. G., & Kikuchi, T. (2008). Estimates of surface roughness length in heterogeneous under-ice boundary layers. *J. Geophys. Res.*, *113(C08030)*, doi:10.1029/2007JC004550.

Shirasawa, K., & Aota, M. (1991). Atmospheric boundary layer measurements over sea ice in the Sea of Okhotsk. *J. Mar. Syst.*, *2*, 63–79, doi:10.1016/0924–7963(91)90014–L.

Shirasawa, K., & Ingram, R. G. (1991). Characteristics of the turbulent oceanic boundary layer under sea ice. Part 1: A review of the ice-ocean boundary layer. *J. Mar. Syst.*, *2(1)*, 153–160, doi:10.1016/0924–7963(91)90021–L.

Spreen, G., Kwok, R., & Menemenlis, D. (2011). Trends in Arctic sea ice drift and role of wind forcing: 1992-2009. *Geophys. Res. Lett.*, *38, L19501*, doi:10.1029/2011GL048970.

Steele, M., Morison, J. H., & Untersteiner, N. (1989). The partition of air-ice-ocean momentum exchange as a function of ice concentration, floe size, and draft. *J. Geophys. Res.*, *94(C9)*, 12739–12750, doi:10.1029/JC094iC09p12739.

Steiner, N. (2001). Introduction of variable drag coefficients into sea-ice models. *Annals of Glaciology*, *33(1)*, 181–186, doi:10.3189/172756401781818149.

Steiner, N., Harder, M., & Lemke, P. (1999). Sea-ice roughness and drag coefficients in a dynamic-thermodynamic sea-ice model for the Arctic. *Tellus*, *A, 51*, 964–978. doi: 10.1034/j.1600–0870.1999.00029.x.

Steiner, N., Holloway, G., Gerdes, R., Häkkinen, S., Holland, D., Karcher, M., Kauker, F., Maslowski, W., Proshutinsky, A., Steele, M., & Zhang, J. (2004). Comparing modeled streamfunction, heat and freshwater content in the Arctic Ocean. *Ocean Modelling*, *6*, 265–284. doi:10.1016/S1463-5003(03)00013-1.

Stroeve, J. C., Holland, M. M., Meier, W., Scambos, T., & Serreze, M. (2007). Arctic sea ice decline: Faster than forecast. *Geophys. Res. Lett.*, *34, L09501*, doi:10.1029/2007GL029703.

Stroeve, J. C., Kattsov, V., Barret, P., Serreze, M., Pavlova, T., Holland, M., & Meier, W. N. (2012a). Trends in Arctic sea ice extent from CMIP5, CMIP3 and observations. *Geophys. Res. Lett.*, *39, L16502*, doi:10.1029/2012GL052676.

Stroeve, J. C., Serreze, M. C., Holland, M. M., Kay, J. E., Malanik, J., & Barret, A. P. (2012b). The Arctic's rapidly shrinking sea ice cover: a research synthesis. *Climatic Change*, *110(3-4)*, 1005–1027.

Sumata, H., Kwok, R., Gerdes, R., Kauker, F., & Karcher, M. (2015). Uncertainty of Arctic summer ice drift assessed by high-resolution SAR data. *Journal of Geophysical Research: Oceans*, *120*, 5285–5301. doi:10.1002/2015JC010810.

Sumata, H., Lavergne, T., Girard-Ardhuin, F., Kimura, N., Tschudi, M. A., Kauker, F., Karcher, M., & Gerdes, R. (2014). An intercomparison of Arctic ice drift products to deduce uncertainty estimates. *J. Geophys. Res. Oceans*, *119*, 4887–4921. doi:10.1002/2013JC009724.

Swift, J. H., Jones, E. P., Carmack, E. C., Hingstone, M., Macdonald, R. W., McLaughlin, F. A., & Perkin, R. G. (1997). Waters of the Makarov and Canada Basins. *Deep-Sea Res. Part II: Topical Studies in Oceanography*, *44*, 1503–1529, doi: 10.1016/s0967–0645(97)00055–6.

Treshnikov, A., & Baranov, G. (1973). *Water Circulation in the Arctic Basin*. Israel Program For Scientific Translations Catalog.

Tsamados, M., Felthams, D. L., Schroeder, D., Flocco, D., Farrell, S. L., Kurtz, N., Laxon, S. W., & Bacon, S. (2014). Impact of variable atmospheric and oceanic form drag on simulations of Arctic sea ice. *J. Phys. Oceanogr.*, *44*, 1329–1353.

Ungermann, M., Tremblay, L. B., Martin, T., & Losch, M. (2017). Impact of the ice strength formulation on the performance of a sea ice thickness distribution model in the Arctic. *J. Geophys. Res. Oceans*, *122*, 2090–2107. doi:10.1002/2016JC012128.

Wamser, C., & Martinson, D. G. (1993). Drag coefficients for winter Antarctic pack ice. *J. Geophys. Res.*, *98(C7)*, 12431–12437.

Yang, J., Comiso, J., Walsh, D., Krishfield, R., & Honjo, S. (2004). Storm-driven mixing and potential impact on the Arctic Ocean. *J. Geophys. Res. Oceans*, *109*. doi:10.1029/2001JC001248.

Table 1: Range of observed and estimated values for atmospheric and oceanic drag coefficients taken from literature. Values reported are for the Arctic Ocean and for regions of interest (see also Figure 1): Lincoln Sea (LS), Beaufort Sea (BS), and Central Arctic (CA).

	Atmospheric (10^{-3})				Oceanic (10^{-3})
Source	range	LS	BS	CA	range
Guest & Davidson (1991)	0.61 - 9.1	-	-	-	-
Lu et al. (2011)	-	-	-	-	1.05 - 22.28
Castellani et al. (2014)	0.88 - 4.66	2.59	1.65	1.65	-
Petty et al. (2017)	1.64 - 2.36	-	1.80	2.20	-
Tsamados et al. (2014)	0.4 - 9	-	-	-	2 - 40

Table 2: Values of the parameters entering equations (10) and (11) for the atmospheric and oceanic drag coefficients in the original formulation from Steiner (2001), and for the optimized run referred to as DRAGS run.

	m_a	m_w	d_a	d_w
Steiner (2001)	1.9×10^{-8}	6×10^{-8}	1.3×10^{-3}	2.6×10^{-3}
DRAGS	0.90423×10^{-8}	3.1226×10^{-8}	1.2839×10^{-3}	2.66110^{-3}

Table 3: Minimum, maximum, mean, and median values of atmospheric and oceanic drag coefficients obtained with the DRAGS run. The last column shows the values of the coefficients used in the CTRL run.

	min (10^{-3})	max (10^{-3})	mean (10^{-3})	median (10^{-3})	CTRL (10^{-3})
c_a	0.8	4.6	1.36	1.27	1
c_w	1.2	13.6	2.82	2.63	5.4

Table 4: Cost function values for the run with original parameters from Steiner (2001), the DRAGS and MEAN runs, and the CTRL run with constant values of oceanic and atmospheric drag coefficients from Castro-Morales et al. (2014). The cost function is computed for ice concentration A, ice thickness H_i, and ice drift $|\vec{v}|$, in summer (S) and winter (W).

	A S	A W	H_i S	H_i W	$\|\vec{v}\|$ S	$\|\vec{v}\|$ W	Sum
Steiner (2001)	1.06	1.32	0.38	0.39	1.01	1.73	5.89
DRAGS	1.12	1.44	0.38	0.34	0.48	0.91	4.67
MEAN	1.16	1.49	0.40	0.33	0.51	0.81	4.70
CTRL	1.21	1.32	0.49	0.35	0.62	0.95	4.94

Table 5: Mean (with one standard deviation) and maximum values of atmospheric and oceanic drag coefficients in March (M) and September (S) of the climatological year of the DRAGS run. Values presented are for the entire Arctic Basin (AB) and for the regions of interest (Figure 1).

	mean $c_a(10^{-3})$	max $c_a(10^{-3})$	mean $c_w(10^{-3})$	max $c_w(10^{-3})$
AB (M)	1.23 (0.32)	3.66	2.50 (1.06)	11.02
AB (S)	1.68 (0.52)	3.34	3.56 (1.52)	9.24
LS (M)	1.66 (0.84)	3.12	4.15 (2.88)	9.17
LS (S)	1.86 (0.91)	3.27	4.53 (2.88)	9.20
BS (M)	1.35 (0.12)	1.74	3.06 (0.42)	4.40
BS (S)	1.83 (0.39)	2.42	4.03 (1.10)	5.91
CA (M)	1.33 (0.12)	2.14	3.02 (0.40)	5.65
CA (S)	1.92 (0.21)	2.86	4.23 (0.61)	7.22
ESS (M)	1.19 (0.08)	1.89	2.50 (0.28)	4.72
ESS (S)	1.64 (0.36)	2.16	3.31 (0.89)	4.60
LapS (M)	0.97 (0.05)	1.31	1.74 (0.16)	2.68
LapS (S)	1.54 (0.24)	1.96	2.92 (0.58)	3.92

Table 6: Mean and maximum values of the atmospheric surface length z_0 for the entire Arctic Basin (AB) and for the regions of interest (Figure 1). The brackets contain the value from Guest & Davidson (1991), their Table 1, closest to our computed value and the corresponding sea-ice category.

	mean $z_0\,(10^{-3})$	max $z_0\,(10^{-3})$
AB	0.53 (0.33 - FYI/MYI very smooth)	27.4 (27.0 - MYI very rough)
LS	2.30 (2.0 - MYI smooth)	17.9 (10.0 - MYI rough)
BS	0.59 (0.33 - FYI/MYI very smooth)	3.81 (7.5 - FYI rough)
CA	0.47 (0.33 - FYI/MYI very smooth)	2.30 (2.0 - MYI smooth)
ESS	0.40 (0.33 - FYI/MYI very smooth)	3.20 (2.0 - MYI smooth)
LapS	0.22 (0.33 - FYI/MYI very smooth)	1.67 (1.3 - FYI smooth)

Table 7: Mean values (with one standard deviation) of sea-ice concentration A, sea-ice thickness H_i (m), sea-ice drift $|\vec{v}|$ (cm s^{-1}) and sea surface temperature θ ($^\circ C$) in September for the DRAGS run (A), the MEAN run (B) and the CTRL run (C). The colors of the cells for the DRAGS run indicate whether the number is larger (red) or smaller (blue) than in the MEAN run. The same holds for the colors of the cells of the MEAN run, but in this case the difference is calculated with respect to the CTRL run.

A	DRAGS					
	AB	LS	BS	CA	ESS	LapS
$\bar{A}$	0.505 (0.326)	0.930 (0.048)	0.514 (0.267)	0.808 (0.036	0.371 (0.176)	0.385 (0.137)
$\bar{H_i}$	1.00 (1.08)	6.62 (4.10)	0.98 (0.60)	1.48 (0.18)	0.56 (0.28)	0.50 (0.21)
$\overline{\|\vec{v}\|}$	6.64 (5.65)	0.60 (0.65)	5.25 (2.97)	2.72 (0.4)	1.68 (0.81)	3.86 (1.07)
$\bar{\theta}$	-0.54 (1.52)	-1.66 (0.02)	-0.42 (1.24)	-1.64 (0.02)	-0.24 (0.92)	-0.77 (0.61)
B	MEAN					
	AB	LS	BS	CA	ESS	LapS
$\bar{A}$	0.511 (0.326)	0.958 (0.027)	0.508 (0.262)	0.818 (0.034)	0.391 (0.175)	0.394 (0.141)
$\bar{H_i}$	1.05 (1.16)	7.86 (3.57)	0.98 (0.61)	1.56 (0.21)	0.60 (0.28)	0.52 (0.22)
$\overline{\|\vec{v}\|}$	6.22 (5.30)	0.11 (0.23)	4.90 (2.55)	2.43 (0.34)	1.57 (0.83)	3.59 (0.94)
$\bar{\theta}$	-0.54 (1.54)	-1.68 (0.01)	-0.39 (1.26)	-1.64 (0.02)	-0.30 (0.90)	-0.76 (0.66)
C	CTRL					
	AB	LS	BS	CA	ESS	LapS
$\bar{A}$	0.329 (0.557)	0.970 (0.017)	0.519 (0.272)	0.854 (0.024)	0.477 (0.195)	0.519 (0.138)
$\bar{H_i}$	1.26 (1.27)	8.46 (3.19)	1.00 (0.66)	1.96 (0.21)	0.77 (0.36)	0.78 (0.28)
$\overline{\|\vec{v}\|}$	5.15 (4.77)	0.02 (0.08)	3.19 (1.92)	1.58 (0.17)	1.30 (0.66)	2.84 (0.83)
$\bar{\theta}$	-0.71 (1.38)	-1.68 (0.01)	-0.49 (1.16)	-1.164 (0.02)	-0.56 (0.76)	1.05 (0.52)

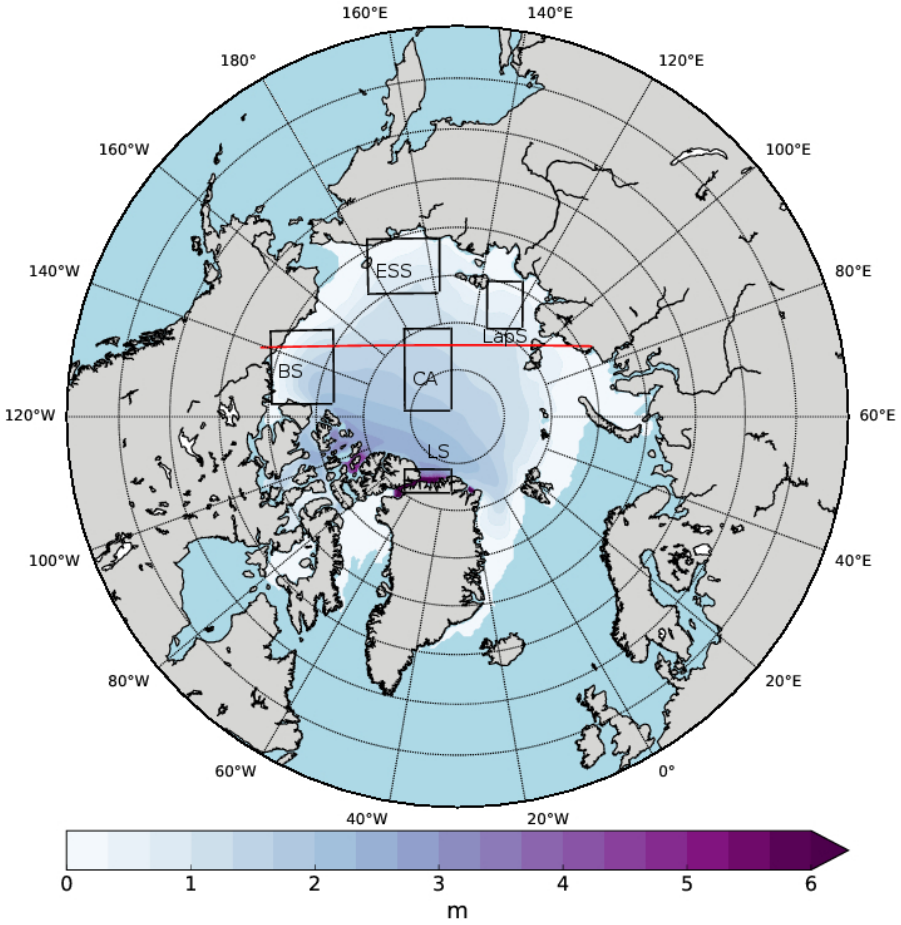

Figure 1: Map of the model domain with in colors the 1990-2010 September climatology for ice thickness obtained with the DRAGS run. The black boxes represent the regions that are relevant in this study: Lincoln Sea (LS), Central Arctic (CA), Beaufort Sea (BS), East-Siberian Sea (ESS), and Laptev Sea (LapS). The red line represents the oceanic transect crossing the Beaufort Sea.

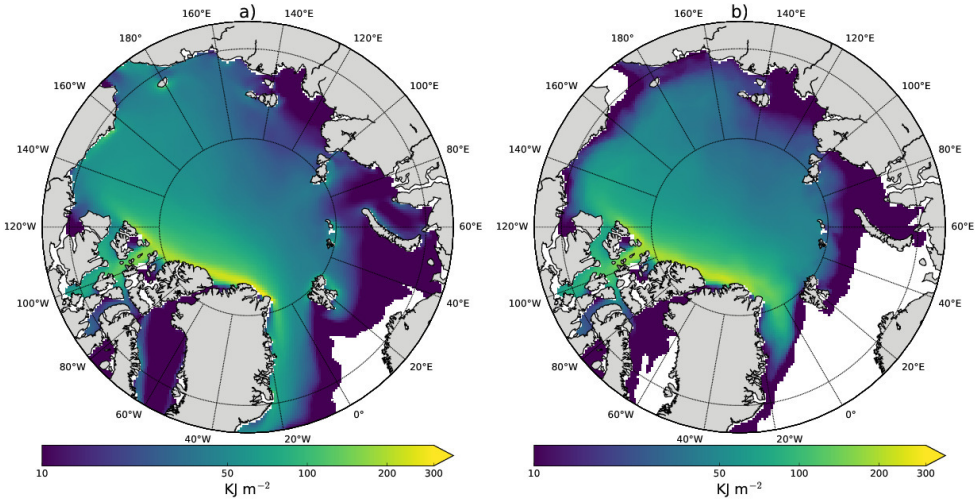

Figure 2: March (a) and September (b) climatologies (1990-2010) of deformation energy.

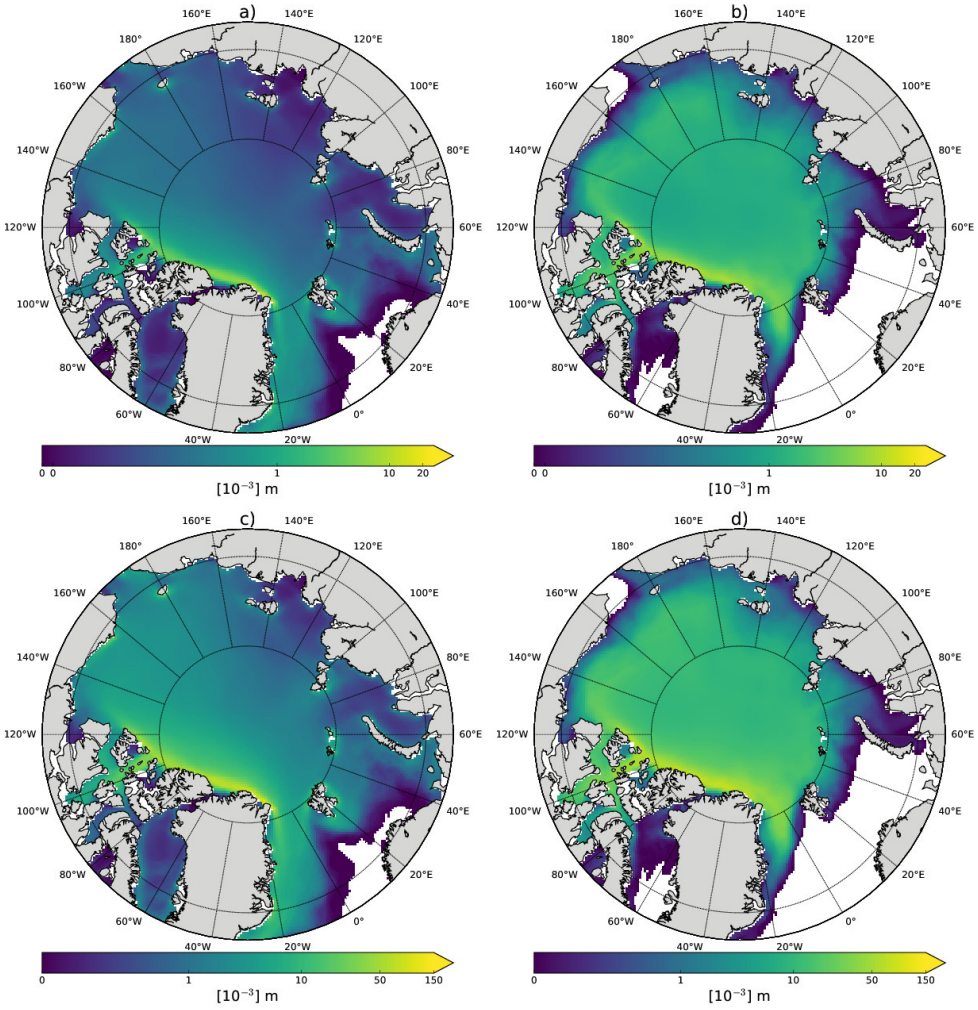

Figure 3: March (left column) and September (right column) maps of roughness length z_0 estimated from the climatologies (1990-2010) of the atmospheric (a-b) drag coefficients and oceanic (c-d) drag coefficients.

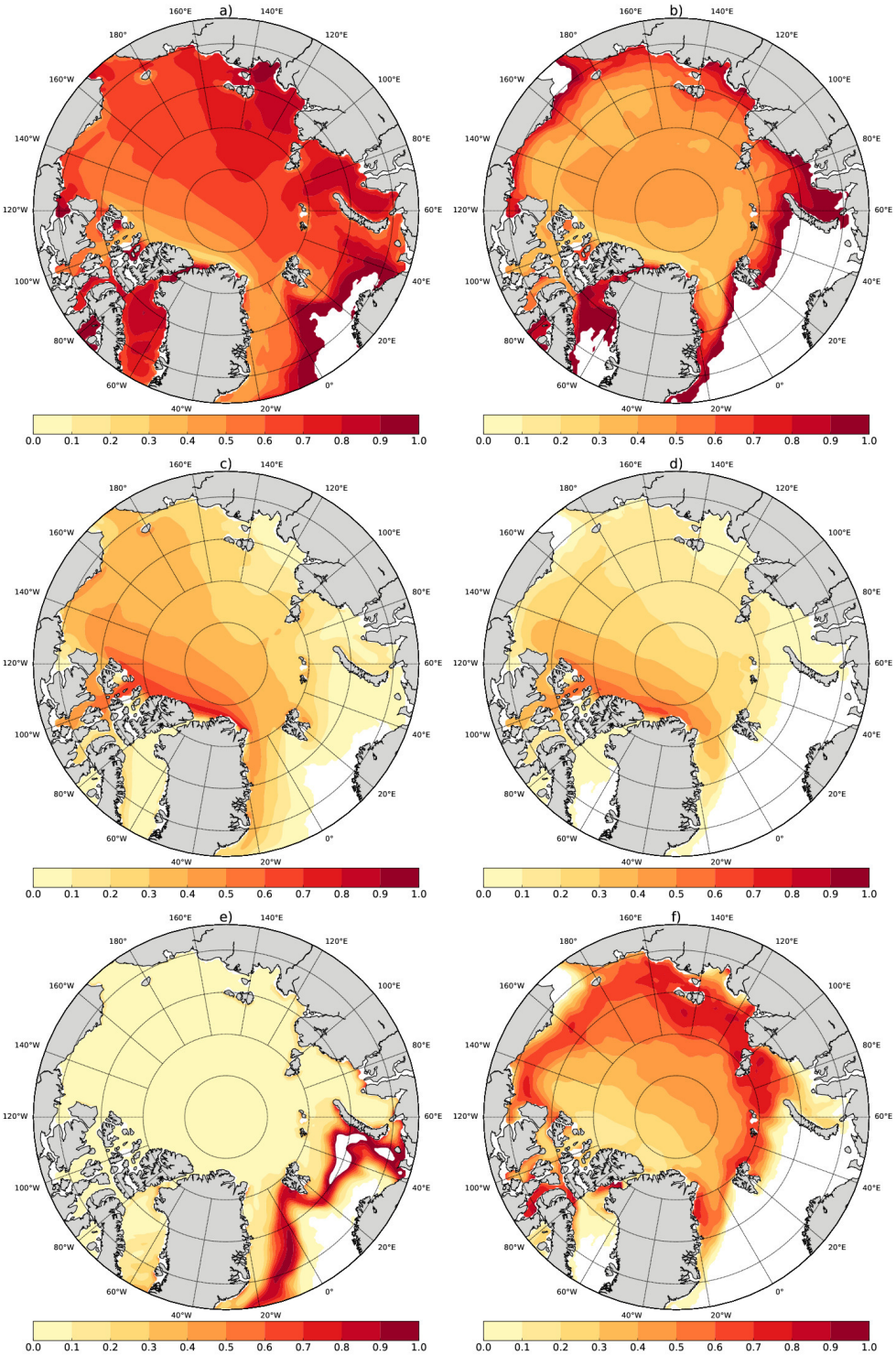

Figure 4: March (left column) and September (right column) contribution of the different terms in equation (10) to the total atmospheric drag coefficient computed as ratio over total atmospheric drag of skin drag term (a-b), deformation energy term (c-d), and ice concentration term (e-f).

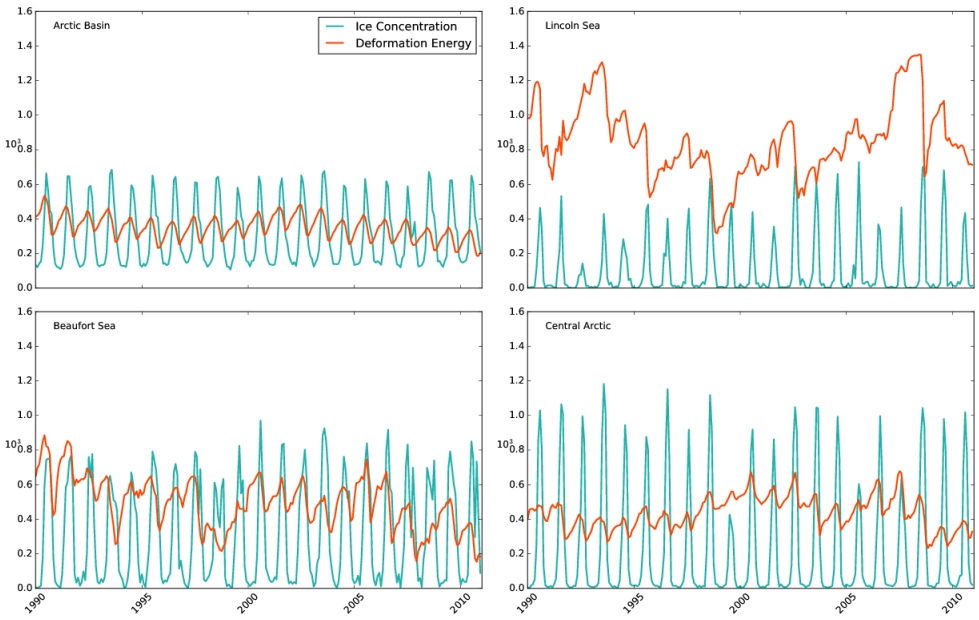

Figure 5: Monthly means of the contribution of deformation energy term (orange line) and ice concentration term (light-blue line) entering equation (10) for the entire Arctic Basin and for some of the regions highlighted in Figure 1.

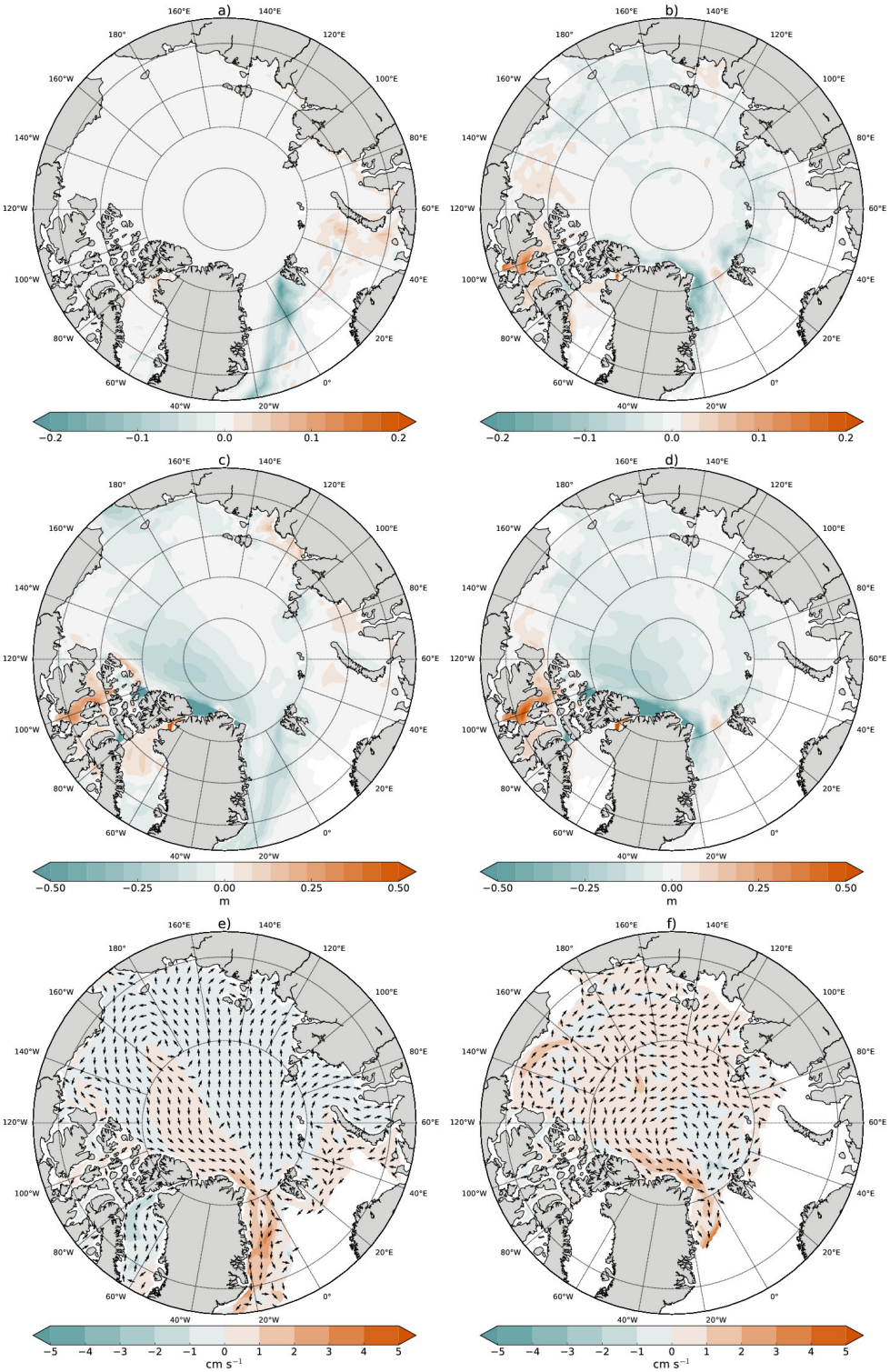

Figure 6: Differences DRAGS - MEAN in March (left column) and September (right column) 1990-2010 climatologies for sea-ice concentration (a-b), thickness (c-d) and drift (e-f).

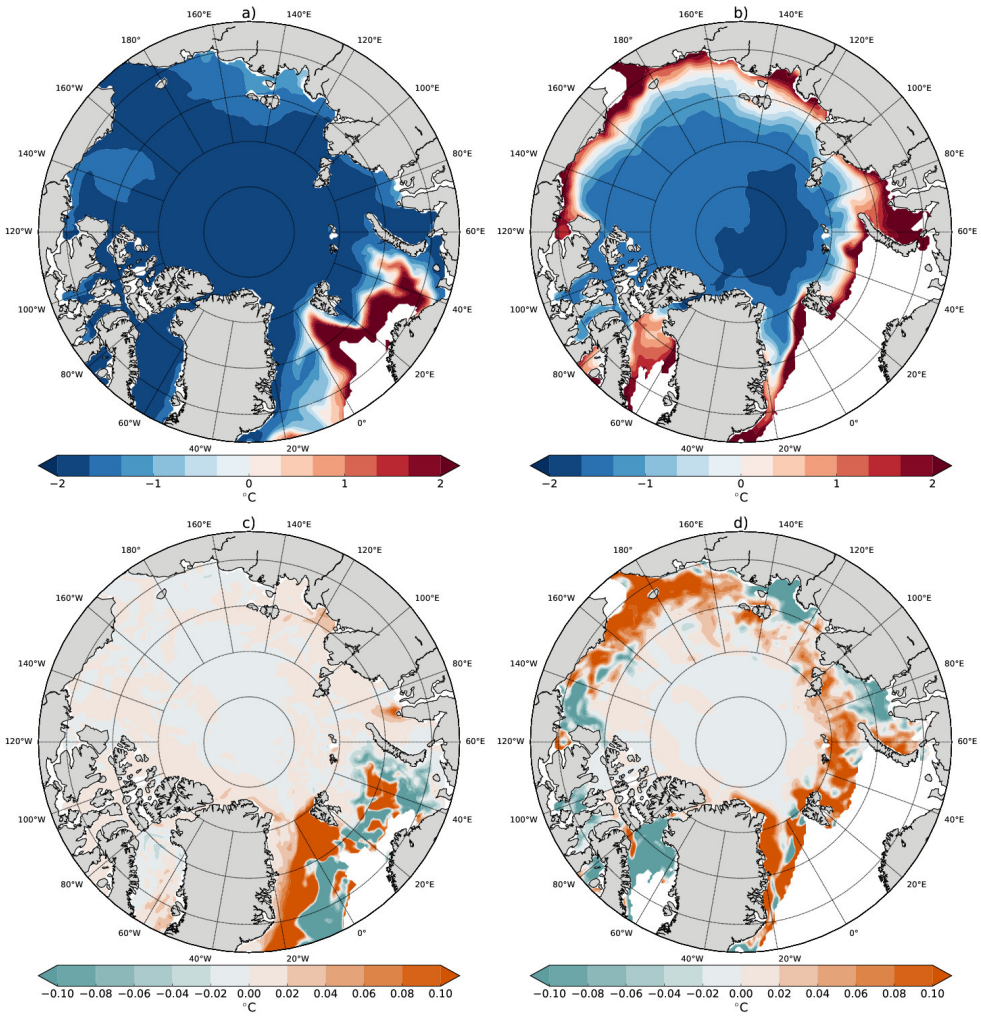

Figure 7: March (left column) and September (right column) sea surface temperatures for the DRAGS run (a-b) and for differences DRAGS - MEAN (c-d).

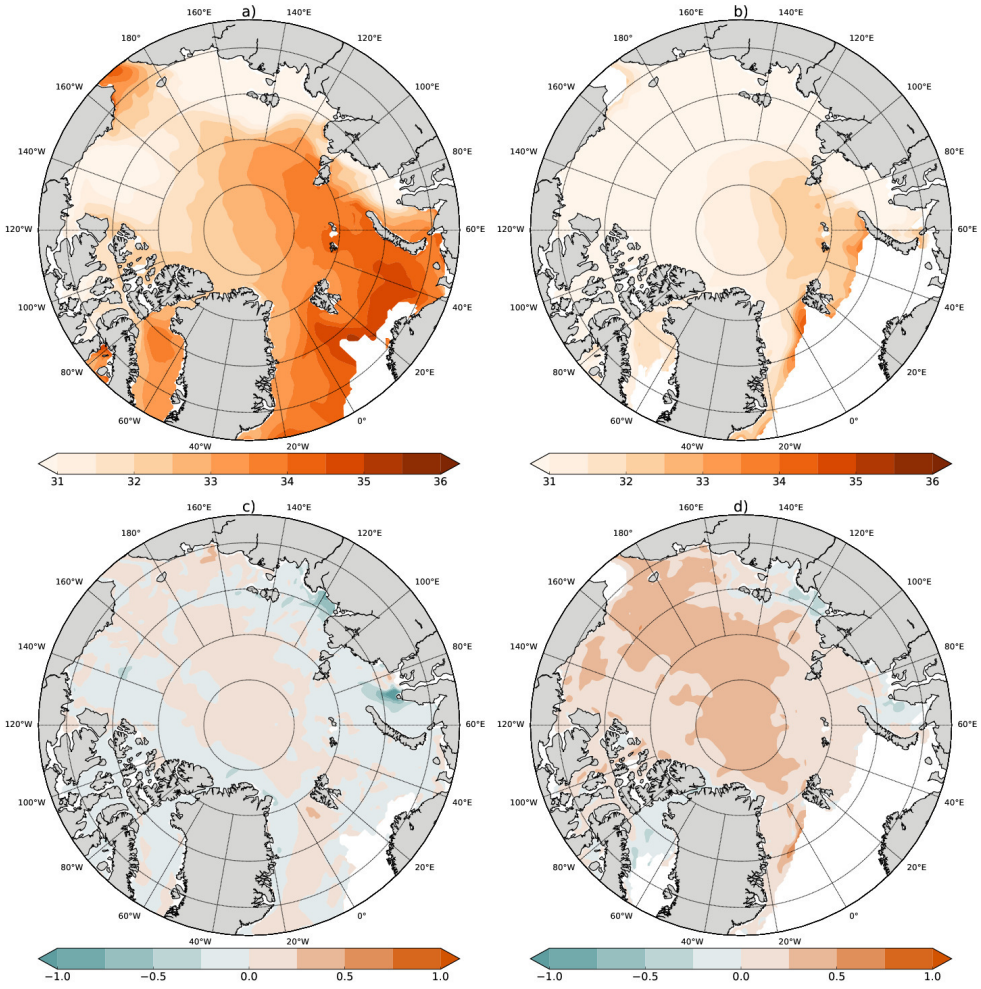

Figure 8: March (left column) and September (right column) surface salinity for the DRAGS run (a-b) and for differences DRAGS - MEAN (c-d).

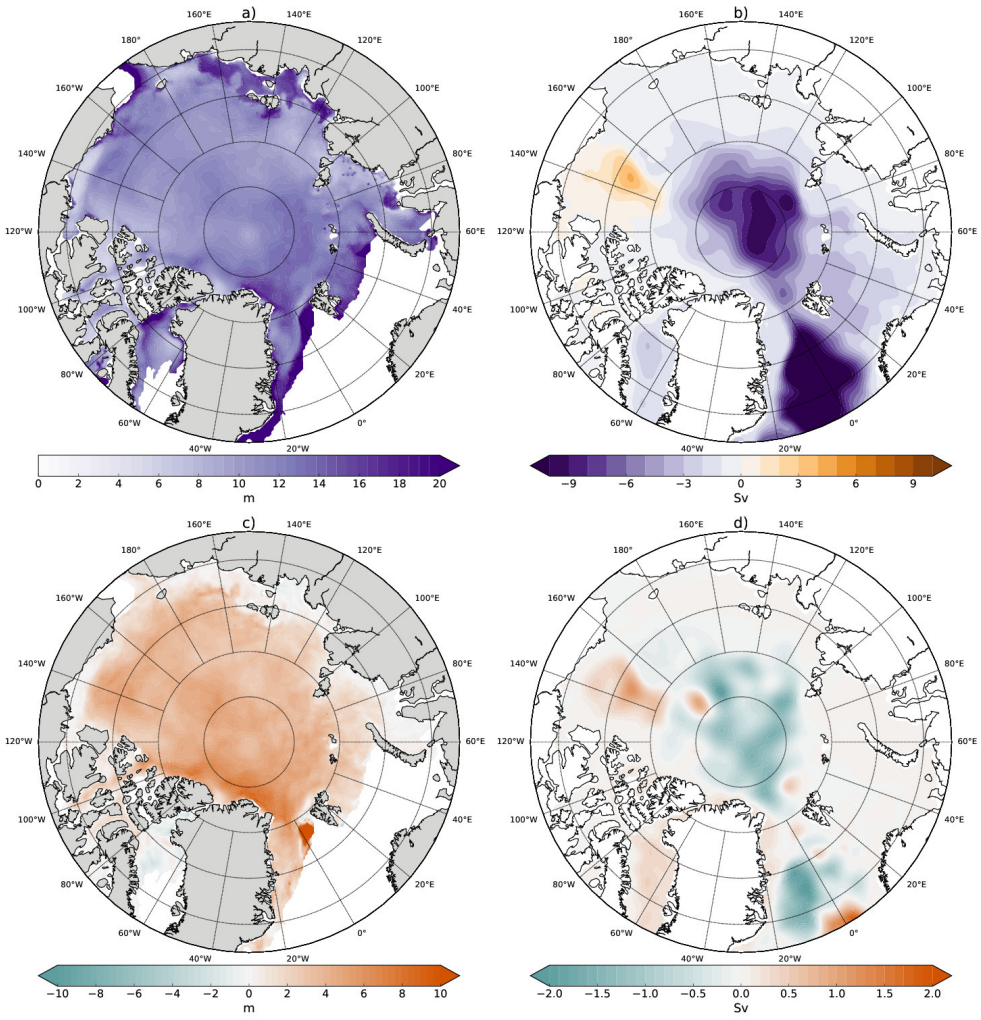

Figure 9: September climatologies of mixed layer depth (left column) and stream function (right column) in DRAGS (a-b), and differences DRAGS - MEAN (c-d)

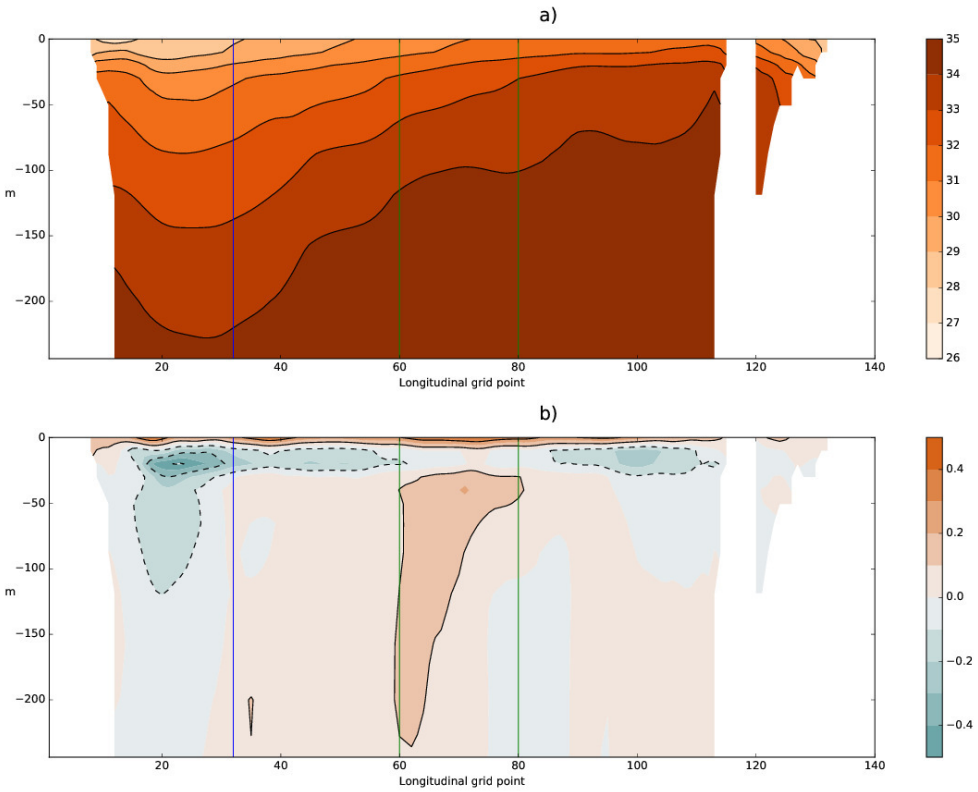

Figure 10: Salinity vertical profile in September along an oceanic transect passing through the Beaufort Sea (Figure 1) for the DRAGS run (a), and differences in salinity vertical profile between DRAGS and MEAN. The blue line represents the right border of the BS region, the green lines enclose the CA region.

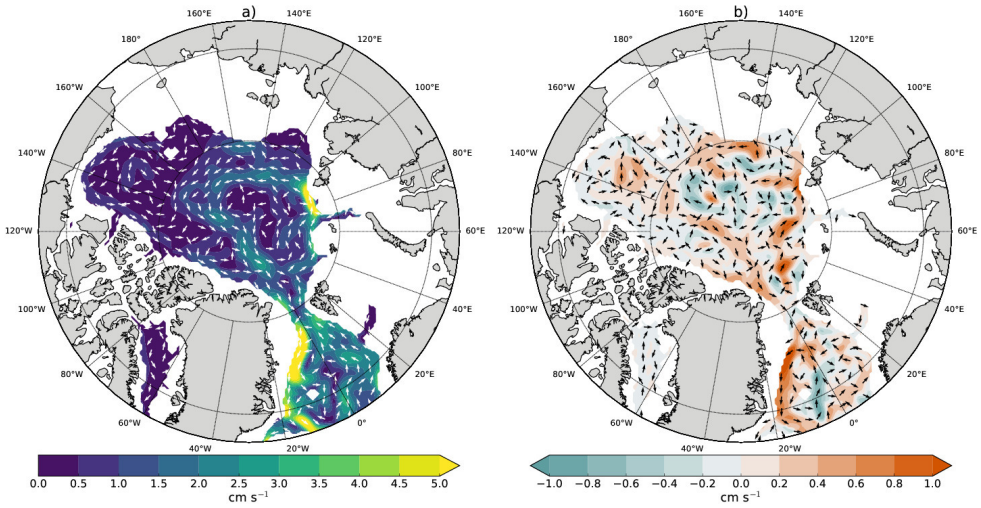

Figure 11: Mid-AW circulation in September in the DRAGS run (a), and differences DRAGS - MEAN (b).

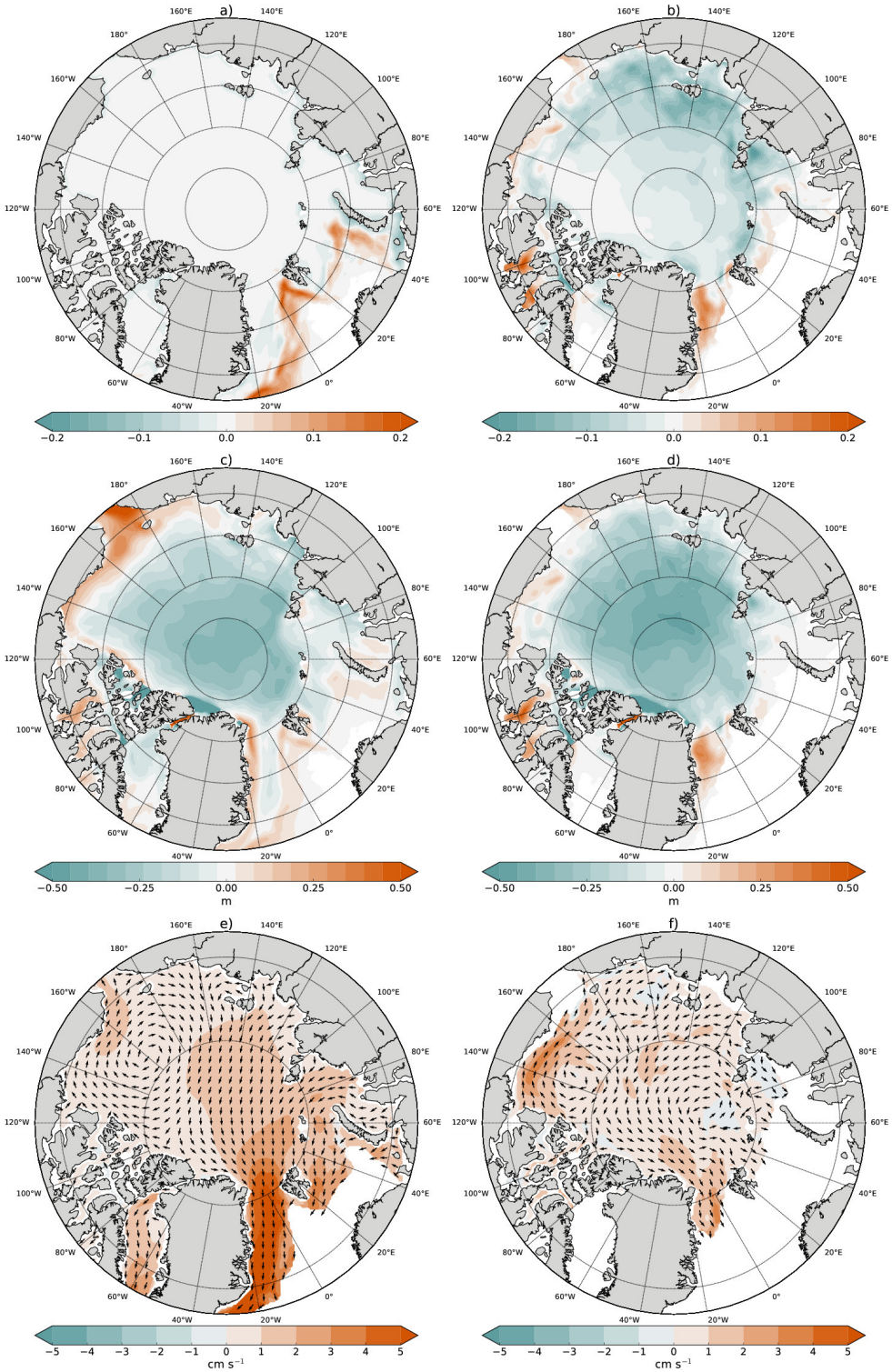

Figure 12: Differences MEAN-CTRL in March (left column) and September (right column) for ice concentration (a-b), thickness (c-d) and drift (e-f).